12

Dusty Rings

M. M. HEDMAN, F. POSTBERG, D. P. HAMILTON, S. RENNER, AND H. -W. HSU

All of the giant planets in the outer Solar System possess rings composed primarily of particles less than 100 microns across. Such small particles are conventionally referred to as "dust grains" regardless of their composition, and so these rings are considered "dusty rings" (as opposed to the more famous main rings of Saturn and Uranus, whose particles are more than a millimeter across). Dusty rings are often very tenuous and so can be much more difficult to observe than Saturn's broad, bright, and dense main rings. Nevertheless, dusty rings are extremely interesting because they have very rich dynamics and are extremely sensitive probes of their environment.

The high surface-area-to-volume ratio of dust-sized grains makes them much more responsive to non-gravitational forces like solar radiation pressure, plasma drag, and torques from the planet's electromagnetic field. Furthermore, sub-millimeter particles can be lost from the ring system on relatively short timescales due to erosion via charged-particle and micrometeoroid bombardment or through ejection by the non-gravitational forces listed above. This means that small particles need to be constantly supplied to these rings from larger bodies, and indeed all of the known dusty rings are associated with larger objects that are the likely sources of dusty debris. The most dramatic example of this is Saturn's E ring, which is clearly supplied by material erupting from beneath the surface of the geologically active moon Enceladus. However, this is a special case, and most dusty rings are instead associated with denser rings (which are composed primarily of millimeter-to-meter-sized particles) or small moons. These objects can serve as dust sources because they are constantly being bombarded by micrometeoroids, and these impacts release fine debris that can escape the weak gravitational fields of these small bodies and go into orbit around the planet. Note that the amount of dust released by this process depends on the size, mass, and regolith properties of the source object, and calculations of the dust production rate based on simple estimates of impact ejecta velocity distributions suggest that source moons that are several kilometers across are the most efficient at producing dusty rings (Burns *et al.*, 1999). While this is consistent with the typical size of moons found within many dusty rings, it is important to remember that the amount of material in a given dusty ring also depends upon how quickly material is transported away from the moon or eroded by various processes.

Regardless of how it is generated, the dust in these rings can transport material between objects and can even deliver samples of solid bodies to a spacecraft. In addition, the relatively short lifetimes of individual dust grains, coupled with the relatively low mass of the rings and their sensitivity to many different forces means that the structure of these dusty systems can change much more rapidly than dense rings. Indeed, several dusty rings have changed substantially over timescales of years to decades, enabling us to observe dynamical phenomena in real time.

In this chapter, we will examine the processes that form and sculpt dusty rings. First, we will provide a brief survey of the known dusty rings, which will demonstrate the rich diversity of dusty systems that surround the giant planets. Next, we will consider the material content of the various dusty rings and discuss the remote-sensing and *in situ* data that have constrained both the sizes and the compositions of the ring particles. Finally, we will examine the various processes that can sculpt dusty material into the wide variety of features that have been observed.

12.1 SURVEY OF THE KNOWN DUSTY RINGS

Chapters 3–6 describe the ring systems of each of the giant planets in detail, including their dusty components. We will therefore just provide very brief surveys of the known dusty rings in order to place all these systems in the appropriate context. Figure 12.1 provides an overview of the four giant planet ring systems.

Jupiter, despite being the largest and most massive planet, has the most tenuous ring system (see Chapter 6 and references therein). Indeed, all of Jupiter's rings probably consist of debris knocked off the surfaces of Jupiter's small inner satellites. This ring system is divided into four components, the Main ring, the Halo ring, and two Gossamer rings. The Main and Halo rings consist of fine debris extending inwards from the orbits of the moons Adrastea and Metis. In the Main ring, this material is confined to a relatively flat sheet, while in the Halo it becomes much more vertically extended thanks to resonant interactions with Jupiter's magnetic field. The two Gossamer rings are an order of magnitude fainter than the Main ring and appear to consist of material launched from the surfaces of the moons Amalthea and Thebe.

Neptune's ring system also appears to consist of almost entirely dusty rings (see Chapter 5 and references therein). However, the optical depths of these rings are significantly higher than Jupiter's rings, and they display a broader range of morphologies. This ring system is dominated by two narrow rings, called the Adams and the Le Verrier rings. While on

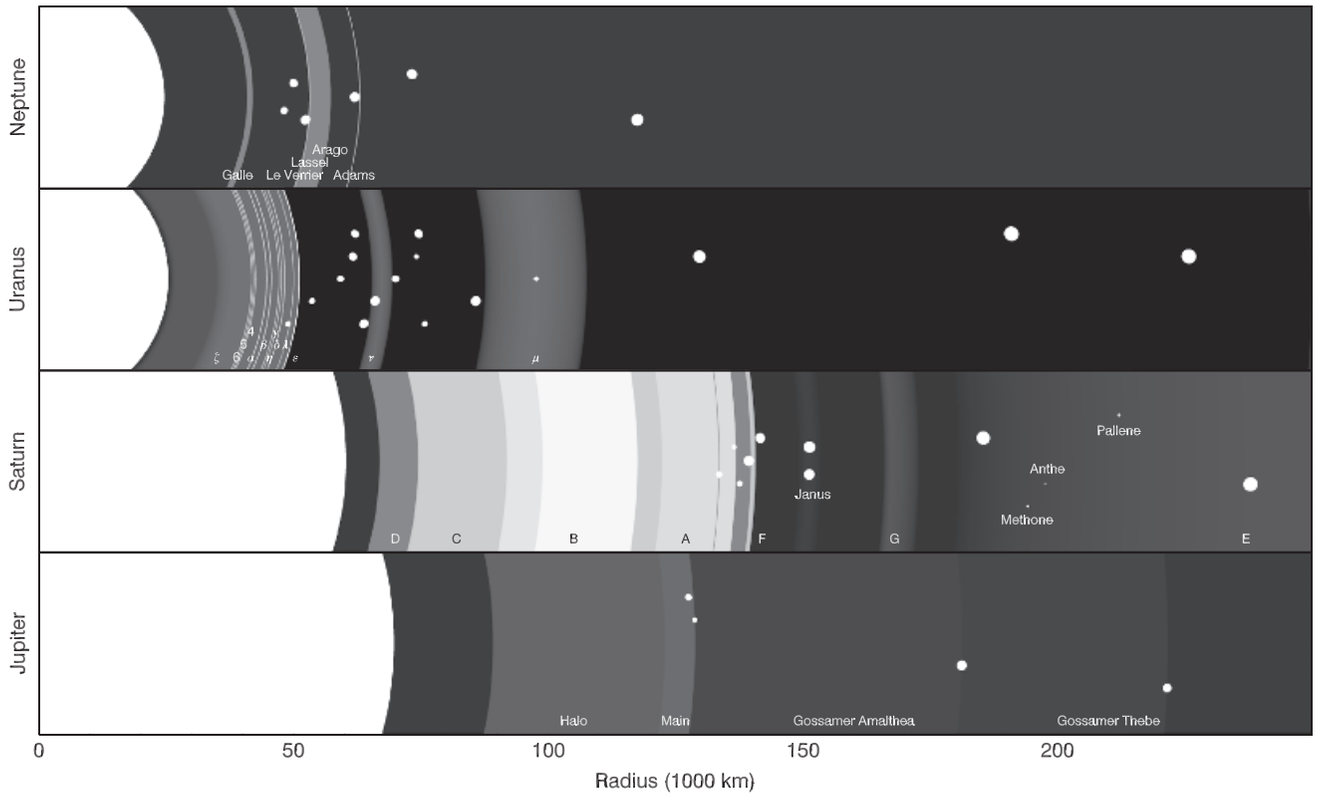

Figure 12.1 Overview of the giant-planets' ring systems, with the various faint rings marked. Note that the graphic showing Saturn's rings marks several moons associated with faint eponymous rings. These graphics do not include Saturn's enormous Phoebe ring.

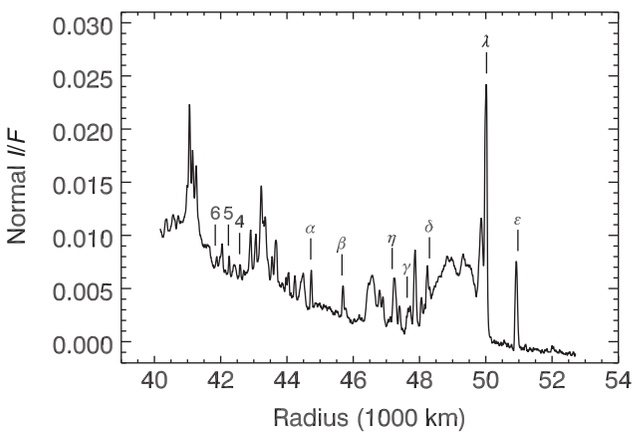

Figure 12.2 Brightness profile of the complex array of dusty features surrounding Uranus' main ring systems, derived from Voyager image FDS 26852.19 obtained at a phase angle of 174°. The letters and numbers mark the locations of the named rings.

average the Le Verrier ring is brighter than the Adams ring, the Adams ring contains a series of longitudinally confined arcs that are so opaque that they can be detected in stellar occultations. In addition, there are more diffuse components of Neptune's rings known as the Galle, Lassell, and Arago rings.

Uranus' ring system includes a suite of narrow dense rings as well as a number of different types of dusty rings (see Chapter 4 and references therein). Exterior to the dense ring system are the μ and ν rings (Showalter and Lissauer, 2006; de Pater *et al.*, 2006b). The μ ring appears to consist of material launched off the surface of Uranus' small moon Mab, while the ν ring may be confined between the orbits of the moons Portia and Rosalind. Interior to the dense rings is the ζ ring, a rather broad sheet of dust whose overall shape and location appears to have changed substantially over the last three decades (de Pater *et al.*, 2006a). Finally, there is a complex array of dust-rich structures scattered among the denser rings, most of which were only clearly seen in a single very high-phase image from the Voyager 2 spacecraft (see Figure 12.2). The most prominent dusty feature in this region is the very narrow λ ring, but there are many additional narrow ringlets and broader structures as well.

Saturn, of course, has the most extensive ring system, and has the most diverse collection of known dusty rings (see Chapter 3 and references therein). Far from the planet, there is the enormous Phoebe ring, which consists of dust knocked off the surfaces of the planet's distant irregular satellites (Verbiscer *et al.*, 2009; Hamilton *et al.*, 2015). The next largest ring is the E ring, which spans of orbits of most of Saturn's larger icy satellites. Cassini observations have revealed that this ring consists primarily of micron-sized particles launched from Enceladus' south pole by that moon's ongoing geological activity (Dougherty *et al.*, 2006; Hansen *et al.*, 2006; Porco *et al.*, 2006; Spahn *et al.*, 2006a; Waite *et al.*, 2006; Kempf *et al.*, 2008, 2010; Ingersoll and Ewald, 2011). Near the inner edge of the E ring are several additional faint rings that likely consist of debris knocked off of smaller moons. The brightest of these is the G ring, which is associated with the small moon Aegaeon (Hedman *et al.*, 2007b, 2010a). Fainter rings are found near the orbits of the small moons Janus, Anthe, Methone, and Pallene. Furthermore, longitudinally confined arcs of material surround Aegaeon, Anthe, and Methone (Hedman *et al.*, 2009a).

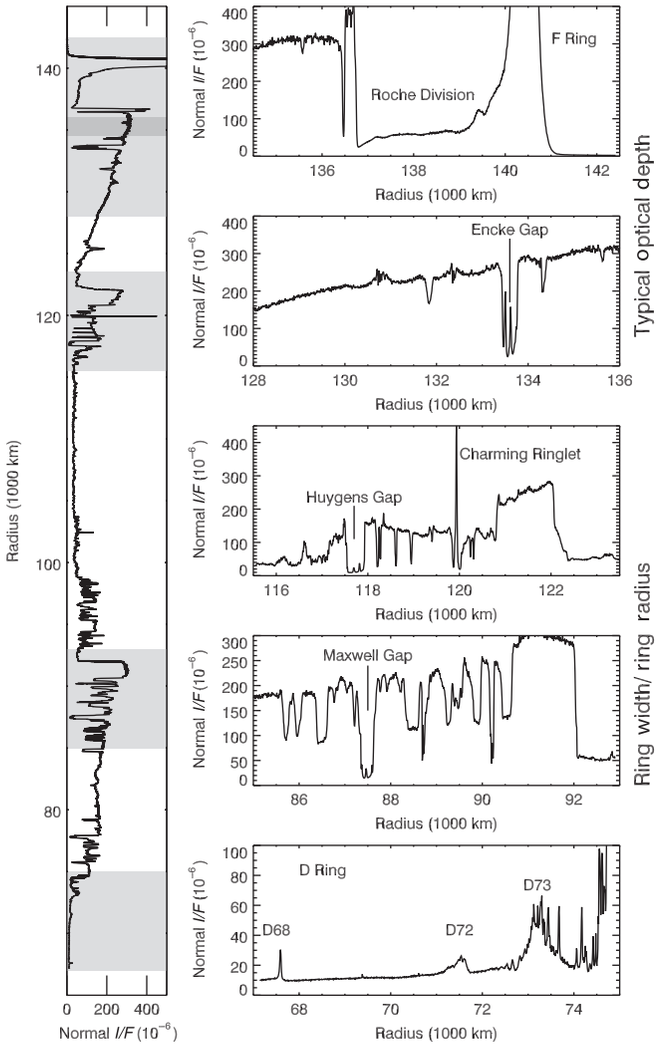

Figure 12.3 Brightness profile of Saturn's rings derived from images obtained by the Cassini spacecraft on day 275 of 2015 at high phase angles (∼137°) and low ring opening angles (∼0.6°), both of which enhance the visibility of dusty material (these images were of the unlit side of the rings, so the nearly opaque B ring appears particularly dark). The panels at right show the locations of dust sheets flanking the rings and several gaps containing dusty ringlets.

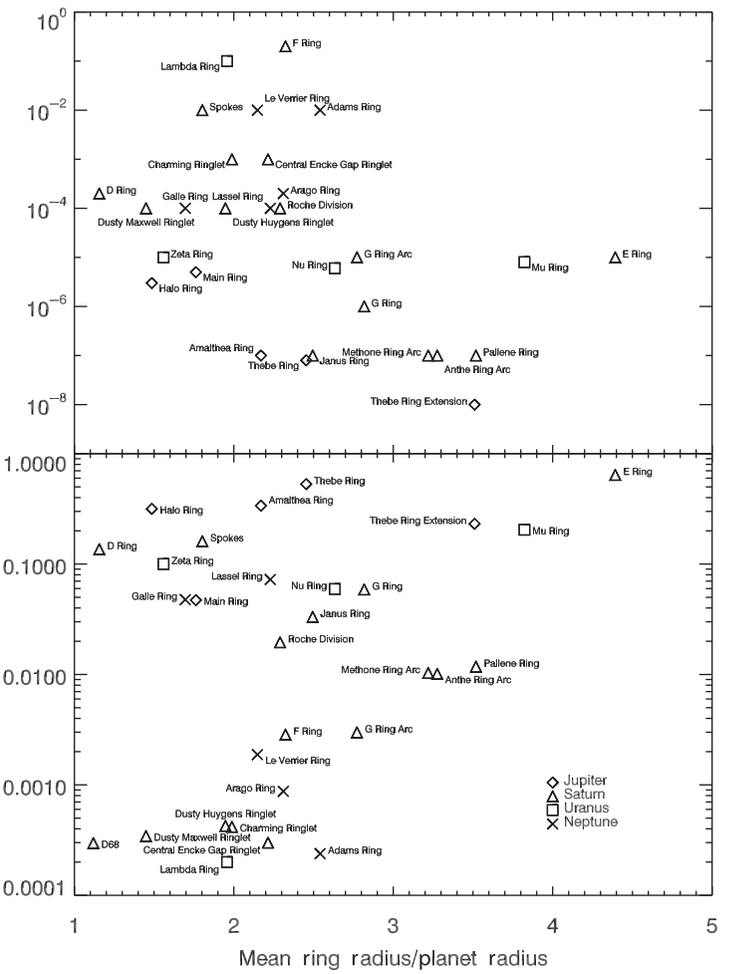

Figure 12.4 The basic properties of dusty rings. These plots show the typical optical depth and fractional width of the various dusty rings as functions of distance from the planet. Again, the Phoebe ring data point is not shown because its optical depth and size are well off the scales of these plots.

Additional dusty rings are found in the vicinity of Saturn's dense main rings (see Figure 12.3). The brightest and most complex of these is the narrow F ring (see Chapter 13), which lies just exterior to the main rings. The region between the F ring and the Main rings is known as the Roche Division, which contains a population of fine particles that are probably derived from those two rings (Burns *et al.*, 1984; Porco *et al.*, 2005). Similarly, interior to the main rings is the D ring, a dust population that contains abundant substructure on a wide range of scales, including three ringlets designated D68, D72, and D73 (Showalter, 1996; Hedman *et al.*, 2007a). Narrow dusty ringlets also occupy several of the larger gaps within the main rings. These include very faint dusty rings in the Maxwell and Huygens Gaps, a much brighter feature in the Laplace Gap (informally designated the "Charming" ringlet), and multiple ringlets within the Encke Gap in the A ring. The Encke Gap ringlets are noteworthy because they show dramatic brightness variations with longitude in the form of discrete clumps whose distribution slowly changes over time (Ferrari and Brahic, 1997; Hedman *et al.*, 2013). Finally, while dust appears to be rare within most of Saturn's main rings, streaks of dust known as spokes are observed over the outer part of Saturn's B ring. The visibility and distribution of the spokes indicate that they are influenced by both Saturn's seasons and the ring's electromagnetic environment (McGhee *et al.*, 2005; Mitchell *et al.*, 2013).

Each of the above rings has distinctive properties and occupies a unique environment, but for the purposes of this chapter it is useful to compare a few basic properties of these rings: their location, optical depth, and fractional radial width. Figure 12.4 plots the parameters for the known dusty rings, which not only illustrates just how diverse these ring systems are, but also clarifies which rings are most likely to be comparable to each other. More specifically, we may identify some basic types of dusty rings.

Broad, distant dusty rings like Saturn's E ring and Phoebe ring, Uranus' μ ring, and Jupiter's Gossamer rings: These rings are found at the greatest distances from their host planets, where

orbital periods are long and the planet's tidal forces are weak. These rings tend to have very low optical depths, and they all probably consist primarily of fine debris released from the surfaces of various moons, which is then dispersed by such non-gravitational forces like solar radiation pressure and plasma drag.

Narrow, distant dusty rings like Uranus' ν ring, Neptune's Adams ring and Saturn's G ring, as well as the faint rings associated with Saturn's moons Janus, Anthe, Methone, and Pallene. These rings also tend to be quite tenuous (with the notable exception of the arcs in Neptune's Adams ring), and like their broader neighbors, they probably consist of material knocked off the surfaces of satellites that is then dispersed by non-gravitational processes. However, several of these rings also contain narrow arcs which likely represent material that is longitudinally confined by co-rotation resonances.

Broad, close-in dusty rings like Jupiter's Main ring and Halo ring, Saturn's D ring, Roche Division and spokes, Neptune's Galle and Lassel rings, and Uranus' ζ ring, as well as the other dusty structures found among Uranus' dense ring system. Compared with the more distant broad rings, these rings tend to have significantly higher optical depths indicative of much higher particle densities. These rings also tend to be less homogeneous, exhibiting brightness variations on a range of scales. At least some of these structures appear to be generated by periodic perturbations from the relevant planet's electromagnetic field.

Narrow, close-in dusty rings like Neptune's Le Verrier ring, Uranus' λ ring, and Saturn's F ring, as well as the various narrow ringlets within the gaps in Saturn's main rings and the D68 ringlet in the D ring. Some of these rings are sculpted by external perturbations. However, this group also includes the most opaque dusty rings and the most tightly confined dust systems, and so they provide the best opportunities to explore interactions among dust particles. Indeed, the remarkably coherent orbital motions of some of these ringlets, as well as the long-lived "clumps" seen in others, may probe these inter-particle interactions.

12.2 THE MATERIAL IN DUSTY RINGS

"Dust" is a very generic term that can be applied to particle populations with a broad range of sizes and compositions (although it typically refers to particles less than 100 microns in radius). Both these parameters influence how efficiently different processes can produce, transport and destroy these particles, and so measurements of particle properties are essential for properly understanding these dusty systems. Of course, any dusty ring is composed of many particles and contains objects with a range of different properties, so in practice we are interested in the *distribution* of particles sizes and materials within these rings.

There are two very different methods for determining the sizes and compositions of the particles in dusty rings. One involves remote-sensing measurements of the rings' spectral and photometric properties, while the other uses *in situ* detectors of the plasma and particles that collide with the spacecraft (see also Chapter 14). These two techniques are very complementary. *In situ* measurements, for example, can obtain very detailed information about the composition of the impacting ring particles, and can detect much lower particle densities than remote-sensing instruments, but these instruments can only obtain data about systems a spacecraft can safely fly through. Remote-sensing instruments provide much less detailed information about the material content of the dust grains, but can provide constraints on the particle size distributions in rings and ring regions that are inaccessible to spacecraft.

12.2.1 Particle Size Distributions of Dusty Rings

Hypervelocity collisions are expected to produce debris with a power-law size distribution, where the local number density of particles with size (radius) between s and $s + ds$ has the form:

$$N_3(s)ds = N_0 s^q ds, \tag{12.1}$$

and the power-law index q has a value of around -3.5 (Dohnanyi, 1969; Colwell, 1996). However, non-gravitational processes that disperse or destroy grains can also be size-dependent and so can cause the observed particle-size distribution to deviate from this particular form. Some of these processes preserve the power-law form of the size distribution and only change the slope q, while others can produce changes in the slope at particular particle sizes. For the sake of simplicity, many studies of the particle-size distributions in dusty rings assume that the size distribution follows a power law and attempt to constrain the index q. While this can be a reasonable approximation for the portion of the size distribution that is probed by a particular experiment, it is important to keep in mind that the full distribution is likely to be more complex.

12.2.1.1 Remote Sensing Observations

For most of the known dusty rings, the only available constraints on the particle-size distribution come from measurements of the ring's brightness as a function of wavelength and lighting geometry. In general, translating brightness measurements into particle properties is a challenging inverse problem because the observed signal in any given situation includes contributions from many different particles. Fortunately, dusty rings are usually so tenuous that one particle is very unlikely to shadow another, and light is unlikely to be multiply scattered between particles before reaching the observer. Hence the observed brightness of a given ring at a given wavelength and viewing geometry should just be the total amount of light scattered by all the individual particles in the relevant part of the ring. More formally, if the incident flux of sunlight on the ring is πF, then the intensity of the light I scattered in a given direction (specified by the scattering angle θ and the azimuthal angle ϕ) can be expressed in terms of an integral over all particle sizes s:

$$I/F = \int N_2(s)\sigma_{sca}(s,\lambda)P(\theta,\phi,s,\lambda)ds, \tag{12.2}$$

where $N_2(s)$ is the surface number density of particles with a size s, σ_{sca} is the size-dependent scattering cross section of the particles, and P is the phase function (also called the scattering function). Conventionally, P is normalized so that its integral

over all solid angles is unity, so σ_{sca} is a measure of how much total light is scattered by the particles. In general, both σ_{sca} and P will depend not only on the particles' size, but also on their composition and internal structure. Even tiny dust particles can be extremely complex aggregates of smaller grains with a variety of different material properties, all of which has implications for their light-scattering properties. However, many of the basic characteristics of the dusty rings' spectra and photometry can be understood by considering the much simpler case of perfect dielectric spheres, where both σ_{sca} and P can be computed using Mie theory or approximated with Fraunhofer diffraction (van de Hulst, 1957; Jackson, 1998).

For example, the known dusty rings exhibit a wide range of spectral slopes when viewed at the low phase angles available to Earth-based observers. As indicated in Figure 12.5, Jupiter's Main ring, Saturn's G ring, and Uranus' ν ring have a red spectral slope across the visible and near infrared. However, Saturn's E ring and Uranus' μ ring possess strong blue spectral slopes at these phase angles. These color differences probably do not reflect variations in the composition of the particles. Instead they can be most easily explained as the result of the E and μ rings having steeper particle size distributions than the other dusty rings.

One of the earliest and most basic findings of light-scattering theory is that a particle of a given size s cannot efficiently scatter light at wavelengths $\lambda >> s$. More quantitatively, one can define a scattering coefficient Q_{sca}, which is related to the scattering cross section by the following expression:

$$Q_{sca} = \frac{\sigma_{sca}}{\pi s^2}. \tag{12.3}$$

For perfect dielectric spheres, Q_{sca} depends only on the particles' complex index of refraction and the non-dimensional size parameter $x = 2\pi s/\lambda = ks$. Figure 12.6 illustrates how Q_{sca} varies with x for a few different values of the index of refraction. While the detailed shapes of these curves differ, they all follow similar trends in that Q_{sca} goes to zero when $x << 1$, and is around 1 or 2 when $x >> 1$, depending on whether the imaginary part of the refractive index is large or small. Note that if the imaginary part of the refractive index is non-zero, then the particle can absorb light as well as scatter it, and so the total cross section σ_{tot} is larger than the scattering cross section, and so one can also define an extinction coefficient as:

$$Q_{ext} = \frac{\sigma_{tot}}{\pi s^2}. \tag{12.4}$$

Figure 12.6 also illustrates a few representative curves for Q_{ext}, which are very similar to the Q_{sca} curves, except that they all asymptote to 2 for large values of x (this distinction between Q_{ext} and Q_{sca} will be considered in more detail below).

Leaving aside the distinctions between Q_{ext} and Q_{sca}, the relatively sharp cutoff in these coefficients means that particles with radii $s < \lambda/2\pi$ have essentially zero cross section, and so we can approximate the integral over all particle sizes in Equation (12.2) with an integral over values of s greater than $\lambda/2\pi$ and replace σ_{sca} with πs^2 times a factor of order unity. Furthermore, at low phase angles P is not a very strong function of particle size, so the brightness of the ring is approximately proportional to the total geometric cross section of all particles with radii larger than $\lambda/2\pi$. In this context, the neutral to red colors of Jupiter's Main ring, Saturn's G ring, and Uranus' ν ring indicate that these rings contain a substantial population of particles more than 1 micron across, which can efficiently scatter light at wavelengths around 2 microns. By contrast, the blue colors of Saturn's E ring and Uranus' μ ring imply that these rings are composed of particles that are too small to scatter light efficiently at near-infrared wavelengths.

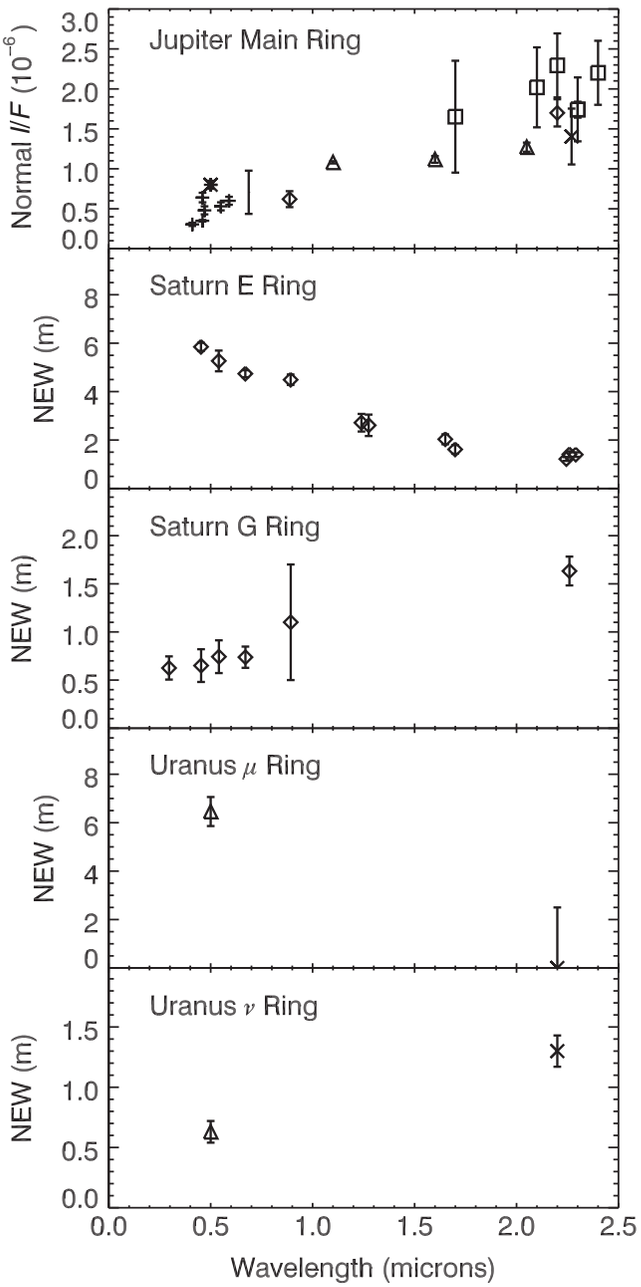

Figure 12.5 Spectra of various dusty rings obtained by Earth-based telescopes, given either in terms of the ring's reflectance when viewed face-on (Normal I/F) or the total radially integrated brightness that would be observed in that geometry (Normal Equivalent Width or NEW). The data on Jupiter's Main ring are from Throop *et al.* (2004), the data on Saturn's E and G rings are from de Pater *et al.* (2004), and the data on Uranus' μ and ν rings are from de Pater *et al.* (2006b).

Remote-sensing and *in situ* data from the Galileo and Cassini spacecraft have not only confirmed that Jupiter's Main rings and Saturn's G ring contain much larger particles than Saturn's E

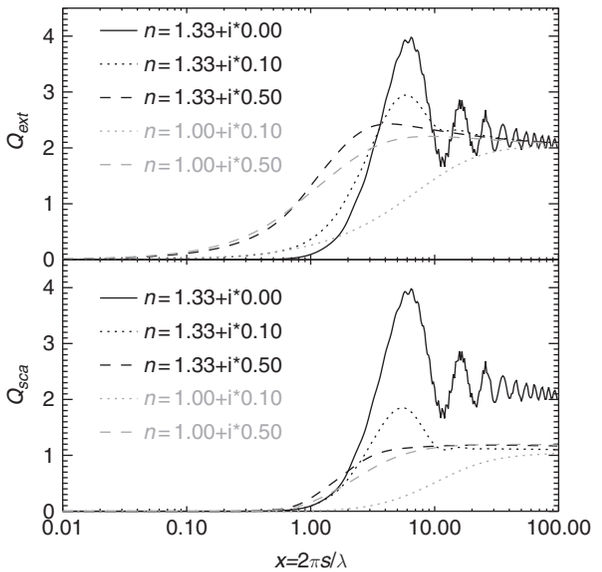

Figure 12.6 Plots of the scattering and extinction coefficients of dielectric spheres with various indices of refraction n, computed using Mie theory. (Note that n here is not the same as the mean motion used elsewhere in this chapter.)

ring, but have also provided much more detailed information about the distribution of particle sizes in the different rings. For remote-sensing, spacecraft-based observations allow the rings to be viewed at high phase angles that are inaccessible to Earth-based observers. One major advantage of observing dusty rings at high phase angles is that the rings appear much brighter in these viewing geometries. Figure 12.7 shows the brightness of Jupiter's Main ring and several of Saturn's dusty rings as functions of the scattering angle θ (i.e. the angle between the incident and scattered light rays). For all of these rings the brightness increases by several orders of magnitude as the scattering angle goes from 180° to 0°. This dramatic increase in brightness means that it is much easier to measure the rings' brightness and spectra at small scattering angles or high phase angles.

In addition to the increase in signal, small scattering angles also make it easier to translate trends with wavelength and phase angle into information about particle sizes. This is because the observed signal comes primarily from diffraction around individual grains. Diffracted light is naturally included in Mie theory calculations, but the gross properties of this component of the scattered light can be more easily obtained and understood using simpler models based on Fraunhofer diffraction. Classical Fraunhofer diffraction theory specifies the amount of light scattered by a perfectly conducting disk, and for a population of such disks with size distribution $N_2(s)$, the predicted reflectance is (Jackson, 1998):

$$I/F = \int N_2(s)\pi s^2 \frac{J_1^2(ks\sin\theta)}{\sin^2\theta} ds, \tag{12.5}$$

where $k = 2\pi/\lambda$, θ is the scattering angle, and $J_1(z)$ is a Bessel function of z.

For obstructions that are not perfect conductors, Mie theory calculations show that the diffracted light at sufficiently high

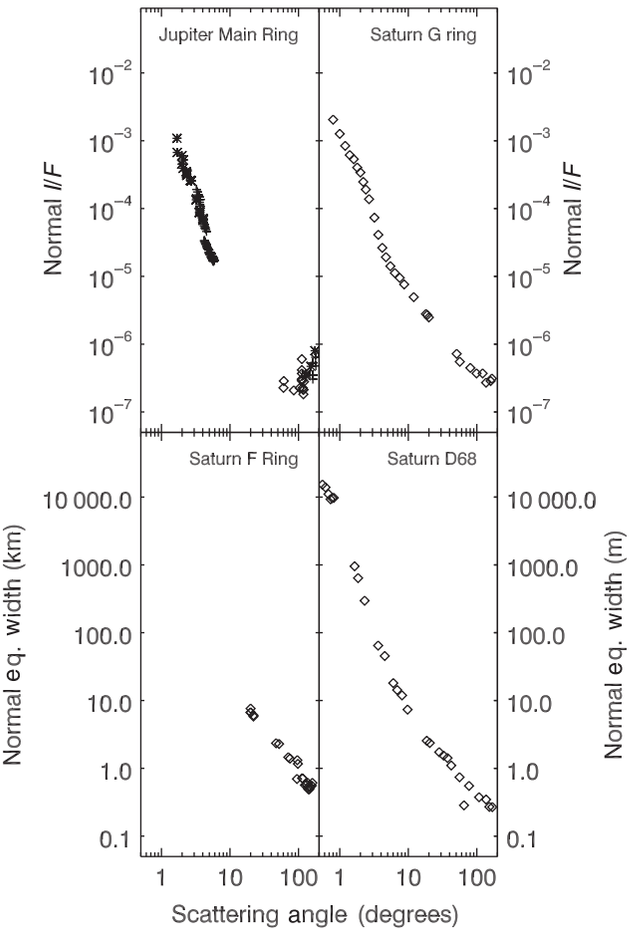

Figure 12.7 Phase curves of dusty rings. Data for Jupiter's Main ring come from Brooks *et al.* (2004) and Throop *et al.* (2004), the data for Saturn's F ring come from French *et al.* (2012), while the data of the D and G rings come from Hedman and Stark (2015).

phase angles has basically the same dependence on θ, but that the magnitude of the signal varies depending on the optical properties of the material. In fact, we can exploit the optical theorem to argue that this numerical factor must equal $Q_{ext}^2/4$, where Q_{ext} is the extinction coefficient described above (Fymat and Mease, 1981). Hence we can approximate the signal scattered by a collection of particles at high phase angles as:

$$I/F = \int N_2(s)\frac{\pi s^2}{4\sin^2\theta} J_1^2(x\sin\theta) Q_{ext}^2(x,\lambda) ds, \tag{12.6}$$

where $x = ks = 2\pi s/\lambda$ is the standard size parameter. Note that $J_1(x\sin\theta)^2$ peaks at $x\sin\theta \simeq 2$, so a particle of a size s scatters light most efficiently when $s \simeq \lambda/\pi\sin\theta$. If θ is sufficiently small, then the peak where $x\sin\theta \simeq 2$ will occur where $x \simeq 2/\sin\theta >> 1$ and $Q_{ext}(x) \simeq 2$. Furthermore, if we assume that over the limited range of particle sizes inside the peak of the Bessel function, the size distribution can be approximated as a simple power law $N_2(s) \propto s^q$, then we can evaluate this integral to obtain

$$I/F \sim \mathcal{C}\frac{\lambda^{q+3}}{(\sin\theta)^{q+5}}, \tag{12.7}$$

where $\mathcal{C}$ is a constant factor that depends on the normalization of N_2 and weakly on the value of q. Thus the trends in the ring's brightness with wavelength λ and scattering angle θ are directly related to the shape of the particle-size distribution where $s \simeq \lambda/\pi \sin\theta$.

Returning to Figure 12.7, we can note that at the smallest scattering angles, none of the measured phase curves follows a perfectly straight line that would be indicative of a pure power-law size distribution. Instead, the phase curves appear to become significantly less steep when the scattering angle falls below a few degrees (this is most noticeable for the data from the G ring and D68). This implies that the particle size distribution becomes significantly less steep, or is cut off around a few tens of microns (Brooks *et al.*, 2004; Throop *et al.*, 2004; Hedman and Stark, 2015).

Further evidence for features in the particle-size distribution can be found by considering the spectra of the dusty rings. According to Equation (12.7), we expect that at sufficiently high phase angles the spectra of dusty rings will be red (brightness increases with increasing wavelength) if the particle-size distribution is shallower than a $q = -3$ power law, and will be blue (brightness decreases with increasing wavelength) if the size distribution is steeper than a $q = -3$ power law. Indeed, the E ring is considerably brighter at short visible wavelengths when it is observed at very high phase angles (Hedman *et al.*, 2009a, 2012), indicating that it has a rather steep size distribution, which is consistent with the low-phase spectral data discussed above.

Other dusty rings, like Jupiter's Main ring and Saturn's F and D rings, do not exhibit consistently blue spectral slopes in the visible and near infrared. This is again consistent with the low-phase spectral data that indicate the particles in this range have a broader range of sizes. However, these high-phase data provide further information about the shape of the particle-size distribution. In particular, all these rings show a clear brightness maximum around 2 microns at scattering angles around 2° (see Figure 12.8). These maxima probably do not reflect any aspect of the particles' composition because their locations all shift to shorter wavelengths as the scattering angle decreases. This is most easily explained as the result of a feature in the size distribution at sizes $s \simeq \lambda/\pi\theta$, which is of order 20 microns. More specifically, since the rings appear red at shorter wavelengths and blue at longer wavelengths, these maxima indicate that somewhere around 20 microns the particle-size distribution goes from being less steep than a $q = -3$ power law to being more steep than such a power law. This is consistent with the phase data mentioned above, which indicate that the size distribution becomes much steeper above 10 microns. Indeed, a variety of light scattering models have found that the spectra of all three rings require a knee or cutoff in the size distribution of these rings at around 10–20 microns (Brooks *et al.*, 2004; Hedman *et al.*, 2007a; Vahidinia *et al.*, 2011; Hedman *et al.*, 2011b).

Finally, recent analyses studying the spectra of the dusty spokes over Saturn's B ring have been able to place new constraints on the particle-size distributions of these unusual dusty

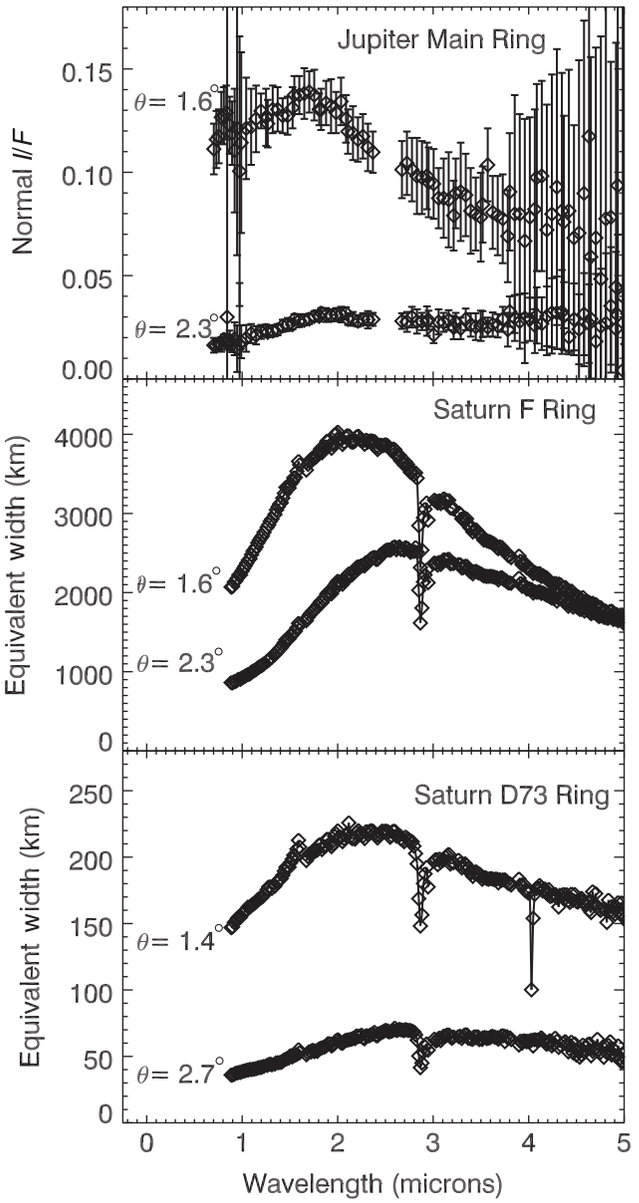

Figure 12.8 Spectra of dusty rings obtained at high phase angles. The data from Jupiter's Main rings are from Brooks *et al.* (2004). The data on Saturn's F ring come from Vahidinia *et al.* (2011), and the D ring measurements come from Hedman *et al.* (in preparation). Note the maxima in all the spectra between 1 and 3 microns, which is indicative of a knee in the size distribution, as well as the narrow dips around 3 microns in Saturn's rings, which are due to the fundamental water-ice absorption band. The dip around 4 microns in the upper D ring spectrum corresponds to an instrumental artifact and is not a real feature in the ring spectrum.

populations (D'Aversa *et al.*, 2010). Since spokes are illuminated by both the Sun and the neighboring dense rings, such analyses are more complex, but again there is a relatively direct mapping between wavelength and particle size. The near-infrared spectrum of the spokes was relatively flat, indicating that the size distribution of particles in these features was broader than previously thought, extending to 10–20 microns with a peak at about 3 microns.

12.2.1.2 In Situ Observations

In situ instrumentation provides another, complementary source of information about the particle sizes of a select number of dusty rings. In fact, Jupiter's tenuous ring system and Saturn's G ring were first detected by *in situ* measurements of the plasma environment by the Pioneer 10 and 11 spacecraft (Fillius *et al.*, 1975; van Allen, 1982) before they were imaged. In both cases, the evidence for these rings' existence came from localized depletions in the number of energetic charged particles striking the spacecraft which arise because these particles were being absorbed by the grains in the dusty rings. More recently, Roussos *et al.* (2008) found depletions in the Cassini measurements of the charged particle density that they interpreted as evidence for an arc of debris near the orbit of Saturn's small moon Methone that was later seen by the cameras (Hedman *et al.*, 2009a).

Besides providing an alternative way to detect tenuous rings, such charged-particle absorptions can provide unique information about the particle-size distributions of these dusty systems. Charged particles are not scattered off the surface of dust grains, but are instead absorbed in their interiors. The magnitude of the absorption therefore depends on the total mass of material in the ring, and so is more sensitive to the larger particles in these ring systems than optical remote-sensing observations. For example, early analyses of the G-ring charged particle absorptions detected by Pioneer 11 indicated that this ring contains particles more than 350 microns across, and that particles bigger than 10 cm were responsible for less than 1% of that ring's opacity (van Allen, 1983, 1987). More recently, Cassini measurements of energetic electrons in the vicinity of the G ring revealed that the arc near the G ring's inner edge contained orders of magnitude more mass than could be present in the visible dust, implying a substantial population of particles more than 10 microns across (Hedman *et al.*, 2007b).

In select cases, instruments can directly detect and characterize individual dust grains that collide with the spacecraft. Since a spacecraft typically moves at speeds in excess of 2 km s^{-1} with respect to the dust particles, capture of intact particles is problematic. Instead, *in situ* detectors are generally devised to measure parameters associated with the high-velocity impact of dust particles onto the instrument. Early dedicated dust impact detectors onboard the Pioneer 10 and 11 spacecraft registered a handful of 10-micron grains in the vicinity of Jupiter (Humes *et al.*, 1974; Kinard *et al.*, 1974). These have been interpreted as arising from outer Jovian satellites (Zook and Su, 1982) or from the Galilean satellites (Zeehandelaar and Hamilton, 2007). More sophisticated instrumentation can obtain information about the size and composition of the dust grains by measuring various properties of the plasma cloud generated by the impact.

Voltage pulses caused by plasma generated from hypervelocity dust impacts onto the spacecraft can be detected by various plasma and radio wave instruments. Indeed, dust impacts were registered by the Voyager plasma instruments during its flybys of the Saturn, Uranus, and Neptune systems (Meyer-Vernet *et al.*, 1986; Gurnett *et al.*, 1987, 1991; Gurnett and Kurth, 1995; Porco *et al.*, 1995), and the Cassini Radio and Plasma Wave Science (RPWS) instrument has been registering dust impacts whenever the spacecraft has passed through the dusty rings (Wang *et al.*, 2006; Kurth *et al.*, 2006; Ye *et al.*, 2014, 2016). Since the mass of an impacting grain determines the total charge of the plasma cloud (Eichhorn, 1976, 1978; Kempf *et al.*, 2006), these measurements can constrain the size distribution of the particles impacting the spacecraft. However, the interpretation of these data is complicated somewhat by the complex antenna–spacecraft coupling mechanisms, as well as uncertainties about the impact plasma production yield (Collette *et al.*, 2014, 2015).

By contrast, instruments like the Dust Detector onboard the Galileo Mission to Jupiter (Grün *et al.*, 1995, 1996; Krüger *et al.*, 2001, 2006, 2009) and the Cosmic Dust Analyzer (CDA) (Srama *et al.*, 2006, 2011; Kempf *et al.*, 2006; Spahn *et al.*, 2006a; Postberg *et al.*, 2006; Hillier *et al.*, 2007b) onboard the Cassini mission to Saturn contain devices known as impact ionization detectors that are explicitly designed to measure the charge of plasma clouds generated by dust impacts into a particular target area. These dedicated dust detectors can observe only dust that strikes the instrument itself from a particular direction, but they have the advantage that the plasma is released in a more controlled environment, enabling more robust measurements of parameters like the impact speed and mass (and for Cassini's CDA, composition as well).

Since the spacecraft has to pass through a dusty ring in order to collect these sorts of measurements, thus far only a few rings have been studied in this way. At Jupiter, the dust detector on Galileo was able to sample the various Gossamer rings and obtain estimates of the particle-size distributions between 0.3 and 3 microns (Krüger *et al.*, 2009). In this size regime, the particle-size distribution in the Gossamer rings appears to be rather shallow, with a power-law index q between -1 and -2. These data are consistent with the remote-sensing measurements of Jupiter's Gossamer rings, which probe slightly larger particle sizes (Showalter *et al.*, 2008). These measurements are also compatible with the high-phase spectra of the Main ring described above, which indicate a rather shallow particle size distribution for particle sizes less than 10 microns (Brooks *et al.*, 2004).

Galileo was able to sample the Jovian rings only near the end of its mission and, for safety reasons, the Cassini spacecraft also avoided passing through many of Saturn's visible dusty rings. However, the spacecraft has passed through the E ring many times, enabling both CDA and RPWS to observe many of this ring's particles. As shown in Figure 12.9, both these instruments find that the particle-size distribution of this ring is steep, with a power-law index typically falling around -4 (Kurth *et al.*, 2006; Wang *et al.*, 2006; Kempf *et al.*, 2008; Ye *et al.*, 2014, 2016). These findings are consistent with above-mentioned remote-sensing observations that indicate this ring has a comparatively small fraction of particles larger than 1 micron in radius.

12.2.1.3 Implications of the Observations

The observations described above do not yet give us a complete picture of the size distribution for any of the known dusty rings. However, these measurements do provide enough information

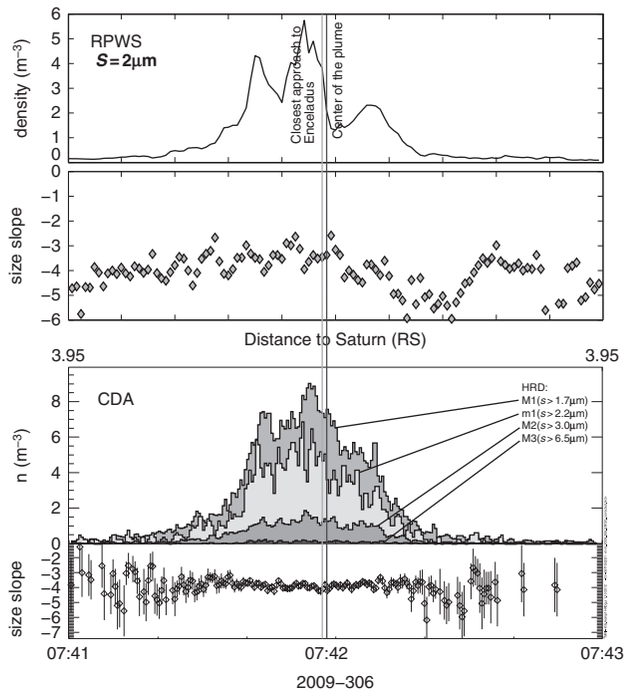

Figure 12.9 Comparison of E ring particle density and size distribution from two *in situ* measurements during the E7 Enceladus close flyby in 2009. The top two and bottom two panels are from Cassini RPWS and CDA measurements, respectively. The size distribution slopes derived from these two measurements are consistent at roughly −4. The RPWS density is scaled down from measurements with a 10 micron threshold and is also comparable with CDA results (adapted from Ye *et al.*, 2014).

to identify a few basic and important features of these dusty systems.

Most of the known dusty rings have spectral and photometric properties that imply they include many particles with radii as large as 10 microns. *In situ* measurements confirm that several of these rings contain detectable populations of "large" (bigger than 100 microns wide) particles. This basic observation is consistent with the idea that most of these rings consist of debris that has been knocked off of larger source bodies by micrometeoroid impacts, because such collisions are expected to generate particles with a broad range of sizes. However, the recent Galileo and Cassini measurements also suggest that the size distributions of many different dusty rings have a sharp knee or cutoff around 10 microns (Brooks *et al.*, 2004; Hedman *et al.*, 2011b; Vahidinia *et al.*, 2011; Hedman and Stark, 2015). It is still far from clear why 10 microns would be a critical size for such a variety of dusty rings around both Jupiter and Saturn. These rings are formed of different materials (silicates at Jupiter, ice at Saturn), occupy a range of different environments, and have very different optical depths, thus there is no obvious commonality that would favor a particular size scale in all of these different contexts.

The remote-sensing and *in situ* measurements also clearly show that the E ring has an unusual size distribution for a dusty ring, with a steep spectral index and a very low fraction of particles larger than a couple of microns across. We now know that these phenomena reflect the ring's atypical origin. Instead of being composed of particles knocked from the surfaces of small moons by impacts, the E ring consists of particles launched from beneath the surface of Enceladus by that moon's geological activity. Enceladus' south polar terrain contains a series of fissures which generate an enormous plume of vapor and tiny particles (Dougherty *et al.*, 2006; Hansen *et al.*, 2006; Porco *et al.*, 2006; Spahn *et al.*, 2006b; Waite *et al.*, 2006). Only a small fraction of these particles (about 5% by mass) are launched fast enough to escape Enceladus' gravity, while the rest fall back onto the moon's surface (Porco *et al.*, 2006; Kempf *et al.*, 2008, 2010; Ingersoll and Ewald, 2011). Furthermore, the plume appears to be stratified, with larger grains concentrated towards its base (Hedman *et al.*, 2009c; Postberg *et al.*, 2011). These trends are consistent with models where the particles are accelerated within the fissures by the flowing gases, a process that is less efficient at accelerating larger grains (Schmidt *et al.*, 2008). Thus the E ring's size distribution can be regarded as a natural consequence of Enceladus' plume dynamics.

However, we should not forget that Uranus' μ ring has a very E-ring-like spectrum, even though its most likely source is the relatively small moon Mab. At the moment, it is unclear why the particles launched from this moon or its vicinity would be much smaller than those coming from Saturn's small moons or the source bodies that supply Uranus' other dusty rings. The μ ring and E ring do both orbit far from their host planets, so perhaps it is reasonable to expect that an E-ring-like balance of precessional forces (cf. Horányi *et al.*, 1992) can also work to spread micron-sized μ ring dust into an observable ring.

12.2.2 The Composition of Dusty Rings

Since the particles in dusty rings come from larger source bodies, the particles in these rings can be regarded as samples of larger objects. Measurements of the dust-grains' compositions can therefore provide information about the origins of the dusty ring material and the makeup of their sources. This is especially interesting for the E ring because those particles come from beneath Enceladus' surface and so can provide information about the internal structure of that moon.

12.2.2.1 Remote-Sensing Observations

Thus far, remote sensing observations have only been able to provide limited information about the composition of dusty rings. At low phase angles, these rings are so faint that it is often difficult to discern diagnostic absorption bands, while at high-phase angles the light is primarily scattered by diffraction, which is relatively insensitive to the particles' composition outside of exceptionally strong absorption bands. For example, spectra of Saturn's D and F rings, as well as of Enceladus' plume, all show a dip at 3 microns that corresponds to the fundamental absorption of crystalline water ice (see Figure 12.8; also Hedman *et al.*, 2007a, 2009c, 2011b; Vahidinia *et al.*, 2011). This implies that all of these rings are composed primarily of water ice. The available spectra of Jupiter's Main rings do not show this absorption (Brooks *et al.*, 2004), demonstrating that these rings are not icy but are instead probably made of more refractory materials like silicates. Hence the spectral data

primarily reveal the dominant constituent of these dusty ring systems.

12.2.2.2 In Situ Observations

The Cassini CDA instrument can provide much more detailed information about the composition of the particles that enter the detector because it can characterize the ions created by a dust impact by the means of time-of-flight mass spectrometry. Because of the above-mentioned concerns for the safety of the spacecraft and the instrument, most of the particles sampled by this instrument come from the E ring. Fortunately, the compositions of E ring grains are especially interesting because they provide unique information about the composition of plume material and therefore can yield insights into Enceladus' interior.

CDA measurements obtained during Cassini's first E-ring crossing in October 2004 quickly confirmed that the particles in the outer E-ring are mostly composed of water ice (Hillier *et al.*, 2007a) and, after more than 10 years of measurement, it is now clear that about 99% of particles detected by CDA in the E ring are dominated by water ice. However, CDA also found that there are significant differences in the compositions of the individual E ring grains, and the mass spectra from CDA can be categorized into at least three distinct families (Postberg *et al.*, 2008, 2009).[1]

- **Type I particles** About 65% of all particles above the detection threshold in the E ring core (close to Enceladus' orbit) belong to this group, increasing to even higher fractions with decreasing particle size. These grains appear to be composed of nearly pure water ice because their mass spectra are dominated by mass lines caused by water cations $(H_2O)^n(H_3O)^+$, $(n = 0{-}15$; see Figure 12.10). Na^+ and K^+ and their respective water cluster ions $(H_2O)^n(Na,\ K)^+$ are often present and form the only non-water mass lines. Even so, these lines imply only very low concentrations of alkali salts with Na/H_2O ratios in the order of 10^{-7} (Postberg *et al.*, 2009).
- **Type II particles** Type II spectra represent the second most abundant E ring family (∼25%) and in most cases show the same characteristic as Type I with an additional distinct feature between mass 27 and 31 which represents more than one species (Postberg *et al.*, 2008). In many cases additional non-water signatures appear and the peaks generally are broader than in the case of Type I or III particles. The additional mass lines are most likely due to various organic compounds. The fraction of organics and the exact composition of the organic species can vary dramatically among the different grains. Furthermore, while organic signatures are the most prominent non-water species, sometimes contributions from silicates and salts may be present. Most Type II spectra are salt-poor, but 10% of all Type II spectra appear to contain higher salt abundances, similar to Type III spectra. Type II

[1] A small fraction (about 1%) of particle spectra detected in the E ring show little evidence for water ice. These are often referred to as Type IV particles and have a widely variable mineral composition. Even though these particles were detected when the spacecraft was in the E ring, these probably are not part of that ring because they were only detected when the pointing of CDA was insensitive to prograde grains with moderate eccentricity and inclination. Furthermore, the great variation in mass spectra indicates a multitude of different sources. Indeed, some of these particles may be interstellar grains (Altobelli *et al.*, 2016).

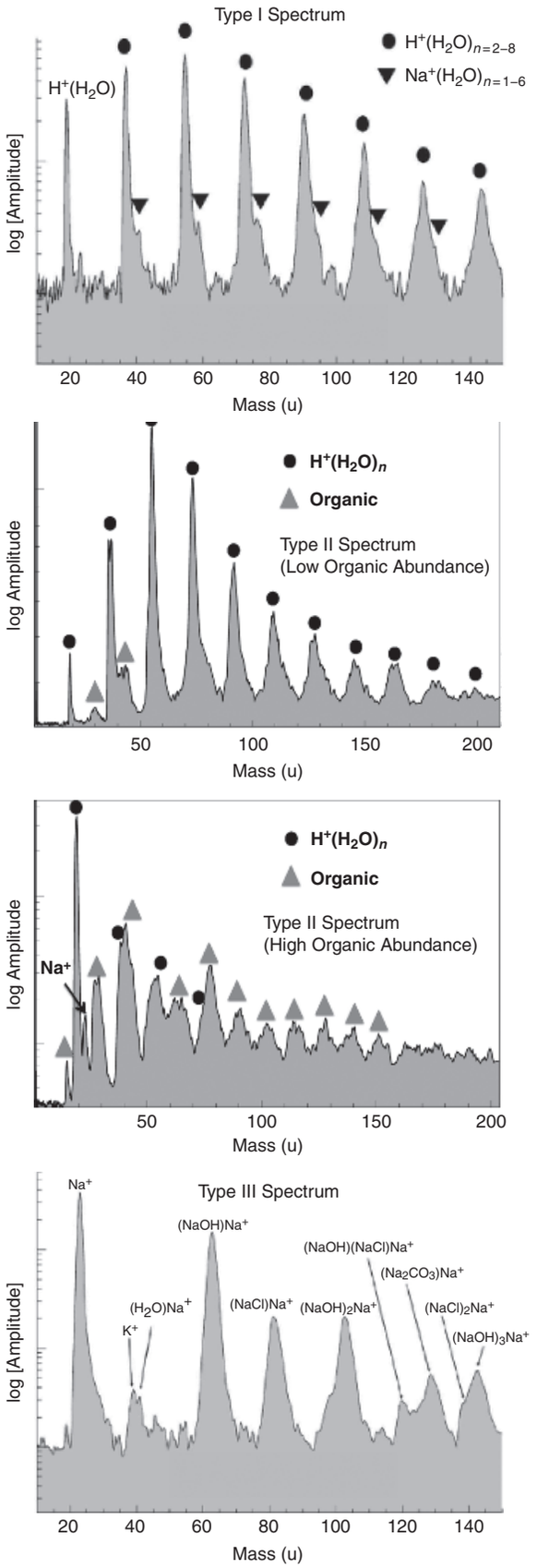

Figure 12.10 Representative mass spectra of the different types of E ring particles. Note the two Type II spectra correspond to low and high abundances of organic species, and that the grain with large amounts of organics also contains a peak that can be attributed to sodium.

Tiscareno, M. S., & Murray, C. D. (Eds.). (2018). Planetary ring systems : Properties, structure, and evolution. Cambridge University Press.
Created from Glenn-ebooks on 2026-02-22 14:34:37.

particles occur more often at higher total ion yields, implying they are larger on average than Type I particles.

- **Type III particles** This family of $\sim$ 10% of E ring spectra exhibits a totally different pattern of mass lines than the other two (see Figure 12.10). In contrast to Type I and II particles, the water cluster peaks $(H_2O)^n(H_3O)^+$ are absent or barely recognizable. The characterizing mass lines are of the form $(NaOH)^n(Na)^+$ $(n = 0 - 4)$ indicating a Na/H_2O mole ratio well above 10^{-3}. Frequent mass lines of $NaCl–Na^+$ and $Na_2CO_3–Na^+$ reveal NaCl and $NaHCO_3$ and/or Na_2CO_3 as the main sodium-bearing compounds. Ground experiments with analog material indicate an average concentration of 0.5–2% sodium and potassium salts by mass, with K compounds being less abundant by far (Postberg *et al.*, 2009). Impacts of Type III particles have an average ion yield which is several times higher than of Type I particles, implying a considerably larger average size (Postberg *et al.*, 2011).

These distinct compositional families probably have very different origins and/or generation mechanisms. The inferred composition of Type III particles matches the composition expected for liquid water on Enceladus (Zolotov, 2007), which has washed out salts from primordial rock from Enceladus' (probably porous) core (Postberg *et al.*, 2009, 2011; Hsu *et al.*, 2015). Therefore, Type III particles likely represent frozen droplets of subsurface salty water. This would imply that the evaporating water surface lies not far below the icy surface of Enceladus and these grains are dragged out by water vapor that follows the pressure gradient through cracks up to the surface and then are expelled into space (Schmidt *et al.*, 2008; Postberg *et al.*, 2009).

By contrast, the salt poor (or salt free) Type I grains cannot be generated this way. Most of these grains are probably produced from vapor that flows upward inside the ice vents and condenses into ice grains as the gas cools (Schmidt *et al.*, 2008; Yeoh *et al.*, 2015). Whether the vapor stems from evaporating salt water or sublimated ice makes no noticeable difference in their composition, and both mechanisms are likely to contribute. However, most Type I spectra show traces of sodium that are in good agreement with the traces of salts that one expects to find in the gas phase of evaporating salt water (Postberg *et al.*, 2009). A small fraction of these grains may even be derived from micrometeoroid bombardment of the icy satellites embedded in the E ring.

The origin of the organic-enriched Type II grains is the least constrained of the three types. However, their great abundance and frequent detection during Cassini crossings of the Enceladian plume again suggest that Enceladus is their main source (Postberg *et al.*, 2008, 2011; Khawaja *et al.*, 2015). Most of them are salt poor, indicating vapor condensates where, besides water, initially volatile organic compounds have condensed on the grain as the vapor cooled on its way upwards through the ice channels. A small fraction of Type II grains show a drastically enhanced salt content (as Type III grains do). These could be frozen salt water droplets that may have incorporated organic compounds from the Enceladian ocean. Alternatively, organics that initially were in the gas phase could have condensed onto the salty ice grain in the vents. Recently, Postberg *et al.* (2017) found that a small fraction of Type II grains have an especially high abundance of organic molecules with high molecular masses that could have formed from an organic nucleation core.

Another dust population observed by the CDA instrument that can provide information about the E ring's composition are the so-called "stream particles"; high-speed, nanometer-sized dust particles that are not gravitationally bound to the Saturnian system and were seen well before Cassini reached Saturn (Kempf *et al.*, 2005b; Hsu *et al.*, 2012). The sizes and speeds of stream particles are beyond CDA's calibration range, but their properties could be derived using a method that accounts for the solar wind magnetic field and speed, which can strongly influence the dynamics of these small grains (Hamilton and Burns, 1993; Zook *et al.*, 1996). Such analyses reveal that streams of nanometer-sized particles come from both the Jupiter and Saturn system and most likely represent tiny grains of dust that were thrown out of orbit by the planets' electromagnetic fields when they acquired a strong enough positive electric charge (Grün *et al.*, 1992; Hamilton and Burns, 1993; Horányi *et al.*, 1993; Horányi and Juhász, 2000; Kempf *et al.*, 2005b; Hsu *et al.*, 2011, 2012). It is thought that the majority of Saturn's stream particles were part of the E ring before they were ejected into the streams. More specifically, these particles are proposed to be inclusions released from much larger E ring ice grains by the magnetospheric plasma erosion (Hsu *et al.*, 2011, 2015).

These stream particles provide unique information about the E ring's composition because, unlike the water-ice-rich particles found in the E ring itself, many Saturnian stream particles appear to have silicon as a major constituent (Kempf *et al.*, 2005a; Hsu *et al.*, 2011, 2015). Silicon-rich nanoparticles could be more likely to be ejected as stream particles than water ice nanograins because they are charged more positively and have higher resistance to plasma sputtering erosion (Jones *et al.*, 2008; Hill *et al.*, 2012; Hsu *et al.*, 2011). Assuming these refractory nanoparticles do come from the E ring (which is consistent with the current observational evidence), then they provide information about rocky material carried aloft by Enceladus' geological activity. In this context, the most remarkable aspect of the stream particles is they are almost metal free, indicating their composition to be silica (SiO_2) but not typical rock-forming silicates (e.g. olivine or pyroxene). These grains can be interpreted as nanometer-sized silica colloids formed during the cooling of hydrothermal waters in the subsurface ocean of Enceladus (Hsu *et al.*, 2015). Combined with long-term laboratory experiments, the composition and narrow size distribution of these grains have been used to argue for ongoing hydrothermal activities within Enceladus and to place constraints on the temperature, alkalinity, and salinity of Enceladus' subsurface waters (Hsu *et al.*, 2015; Sekine *et al.*, 2015).

The insights gained about Enceladus and its geological activity from detailed studies of the E ring grains clearly demonstrate how much information can be gleaned from the composition of tiny ice grains. Hopefully, future spacecraft missions with dust detectors will be able to study other dusty rings and thereby probe the characteristics of their source bodies.

12.3 SCULPTING DUSTY RINGS

Dusty rings exhibit a broad array of structures that reflect the rich variety of forces acting upon the orbits of their small constituent particles. These perturbations include not only

gravitational forces from Saturn's various moons, but also a host of non-gravitational forces, including solar radiation pressure, plasma drag, and other electromagnetic processes. While the interactions among these various phenomena can be quite complex, in certain cases the role of individual forces can be isolated thanks to the distinctive fingerprints they leave on the ring's structure (see also Chapters 2 and 8–11).

In this section, we will examine some of the processes that shape dusty rings. First, we will consider phenomena that apply nearly constant perturbation forces on ring particles, like plasma drag and solar radiation forces, and discuss how these forces can disperse material from source bodies to form diffuse distant rings like Jupiter's Gossamer rings, Saturn's G and E rings, and Uranus' μ ring. Next, we will describe some structures in broad sheets of dusty material that appear to have been generated by recent ring-disturbing events. Then we will consider the more complicated perturbations on ring material associated with mean motion resonances, which can give rise to longitudinally confined ring arcs in Neptune's Adams ring and several of Saturn's rings, as well as several other structures observed in Saturn's D ring, spokes, and the Roche Division. Finally, we will briefly discuss the densest and clumpiest of the dusty rings, where inter-particle interactions may be important.

12.3.1 Transportation of Dusty Material

A good place to begin exploring the dynamics of dusty rings is with the broad, distant rings that have clear associations with specific moons. Figure 12.11 shows the brightness for several of these dusty rings, and in all cases the peak brightness occurs close to the orbit of a moon that probably represents a major source for the material. However, the ring material is never confined to the relevant moon's orbit. Jupiter's Gossamer rings and Uranus' μ ring all contain material interior to their moon's orbit, while Saturn's G ring extends exterior to its moon's orbit. Saturn's E ring is a special case, with substantial amounts of material both interior and exterior to Enceladus' orbit. However, Jupiter's Thebe ring also exhibits a very faint "extension" of material exterior to its moon orbit in addition to the more prominent inward wing of material (Burns *et al.*, 1999). The substantial radial extents of these rings suggest that some combination of processes is affecting the ring-particles' orbital eccentricities and/or semi-major axes.

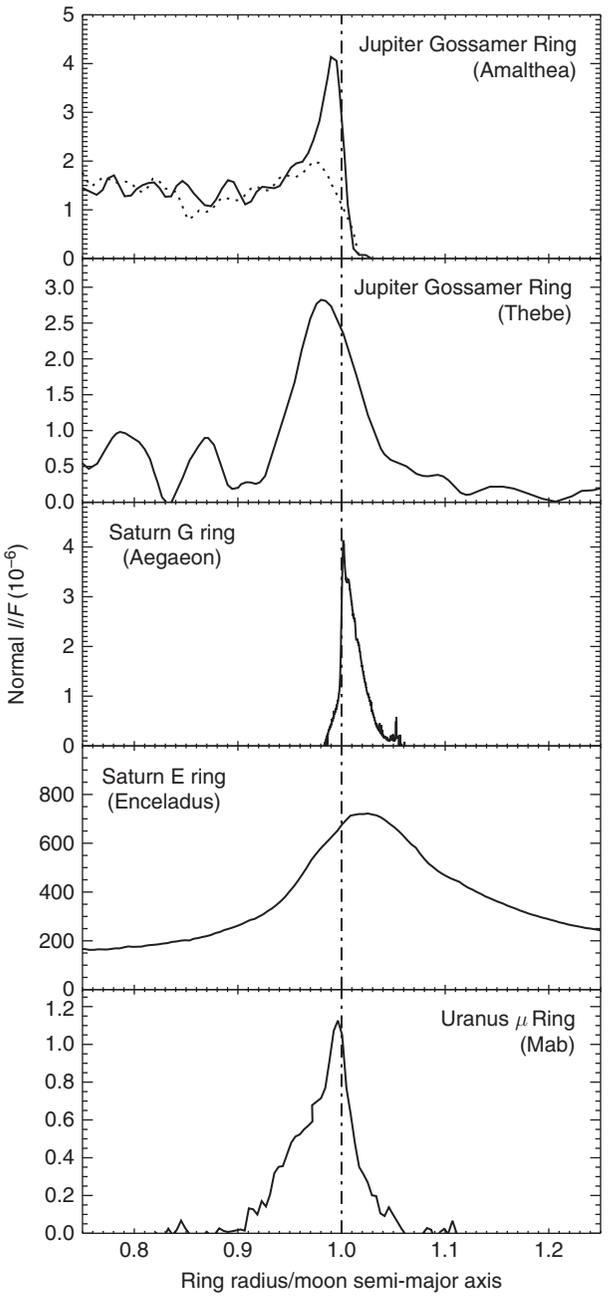

Figure 12.11 Radial brightness profiles of dusty rings associated with particular moons. Each panel shows the ring's brightness as a function of distance from the moon's semi-major axis. The profiles of Jupiter's Gossamer rings come from Showalter *et al.* (2008) and clearly show material extending interior to the orbits of the moons Amalthea and Thebe. Uranus' μ ring shows a similar spread inwards from the orbit of Mab (Showalter and Lissauer, 2006). By contrast, the profile of Saturn's G ring shows that material from this ring preferentially drifts outwards from the orbit of Aegaeon (Hedman *et al.*, 2009a). The E ring shows a similar outward displacement of its peak brightness, although material extends on both sides of its moon (Hedman *et al.*, 2012).

12.3.1.1 Radial Migration Due to Drag Forces

The most direct way for ring material to spread over a range of radii is through secular evolution of the ring-particle's semi-major axes. Indeed, semi-major axis migration is the only way to produce strong asymmetries in the amount of material located interior and exterior to the moon's orbit, because such asymmetries require that the average orbital positions of the ring particles are different from that of their source moon.

According to standard orbital perturbation theory (see Chapter 2), changes in semi-major axis correspond to changes in orbital energy, so in order for a particles' semi-major axis to change over time, the perturbing force must do work on the orbiting particle. Hence, a force that pushes the ring particles forward along their orbits will cause those particles to gain orbital energy and their orbital trajectories to spiral outwards away from the planet. Similarly, a force that opposes the particles' orbital motion will cause the particles to lose orbital energy and spiral inwards towards the planet.

In principle, a number of different processes could give rise to forces that would cause the particles' semi-major axes to drift (see, e.g., Section 12.3.1.4). However, in practice, only two processes are expected to produce azimuthal forces that would cause the semi-major axes of a substantial fraction of the observable ring particles to move in one direction: plasma drag and Poynting–Robertson drag. Plasma drag is momentum exchange with ions in the planet's magnetosphere (Grün *et al.*, 1984). Unlike the ring particles, which orbit the planet at nearly the Keplerian rate, magnetospheric ions are tied to the planet's magnetic field and so orbit at close to the planet's spin rate. For all of the dusty rings shown in Figure 12.11, the planetary rotation rate Ω_P is faster than the local orbital rate n and so the ions tend to hit the dust grains from behind, accelerating the particles and causing them to spiral outwards away from the planet. By contrast, Poynting–Robertson drag arises because a moving object will scatter light asymmetrically along its direction of motion. This produces a back-reaction on the particle which always acts against the particle's forward motion, and so will cause the particle to spiral inwards towards the planet (Burns *et al.*, 1979).

Since Poynting–Robertson and plasma drag act in opposite directions for the rings considered here, the tendency of the material to spread preferentially interior or exterior to the moon's orbit should depend on the relative strength of these two forces. More specifically, for particles on low-eccentricity orbits, the average time rate of change of the particles' semi-major axis a is proportional to the average azimuthal component of the perturbing force $\langle F_\lambda \rangle$ (positive being in the direction of orbital motion):

$$\left\langle \frac{da}{dt} \right\rangle = 2an \frac{\langle F_\lambda \rangle}{F_G}, \tag{12.8}$$

where a and n are the particle's semi-major axis and mean motion, and $F_G = GM_P m/a^2$ is the central component of the planet's gravitational force. While the relationship between the orbital evolution rate and the perturbing force becomes somewhat more complex if the particles have non-zero orbital eccentricities, it remains the case that the orbit-averaged da/dt is proportional to the perturbing force.

For Poynting–Robertson drag, the average azimuthal component of the force acting on a particle of size (radius) s is given by the expression (Burns *et al.*, 1979)

$$\langle F_{PR} \rangle = -\pi s^2 \left(\frac{3}{2} \frac{S}{c} Q_{PR} \right) \frac{na}{c}, \tag{12.9}$$

where S is the total solar energy flux, c is the speed of light, and Q_{PR} is an efficiency factor related to the extinction and scattering coefficients described above ($Q_{PR} = Q_{ext} + Q_{sca}\langle \cos\theta \rangle$, where the last term is the average of the $\cos\theta$, weighted by phase function, see Equation 4 in Burns *et al.*, 1979, and is typically of order unity. For plasma drag, the expression for the force depends somewhat on the temperature and density of the plasma. However, for tenuous, cold plasmas and particles on nearly circular orbits, the azimuthal force on each particle due to momentum exchange between the plasma and a particle of size (radius) s is simply (Grün *et al.*, 1984)

$$\langle F_{pl} \rangle = +\pi s^2 \rho_i w^2, \tag{12.10}$$

where ρ_i is the local plasma mass density and $w = a(\Omega_p - n)$ is the plasma velocity relative to the dust grains. For denser and hotter plasmas, collective effects allow the particle to interact with a larger volume of plasma, and so the relevant force can be enhanced. Note that the positive sign on this force assumes that the dust is located outside the synchronous radius where $\Omega_p = n$.

Both plasma drag and Poynting–Robertson drag forces are proportional to the cross sectional area of the particles. Since F_G is proportional to the particles' total mass, this means that both these forces are inversely proportional to the particle size. Hence small particles will migrate faster than large ones, which is sensible, but the ratio of the two perturbing forces is relatively insensitive to particle size, so all particles tend to move in one direction or the other depending on the relative strengths of these drag forces. Indeed, we can define a ratio of these forces

$$\mathcal{R}_F = \frac{\langle F_{pl} \rangle}{\langle F_{PR} \rangle} = \frac{2}{3} \frac{1}{Q_{PR}} \left(\frac{a_p}{1\text{AU}} \right)^2 \frac{c^2}{S_0} na(\Omega_p/n - 1)^2 \rho_i. \tag{12.11}$$

Note that we have used the equality $S = S_0(1\text{AU}/Ra_p)^2$, where $S_0 = 1.36$ kW m^{-2} is the solar flux at Earth's orbit and a_p is the planet's distance from the Sun. If $\mathcal{R}_F$ is less than 1, then Poynting–Robertson drag overwhelms plasma drag and the particles should spiral in, and if $\mathcal{R}_F$ is greater than 1, then plasma drag is stronger and the particles spiral outwards.

There is one dusty ring that is certainly in the Poynting–Robertson drag-dominated limit: Saturn's Phoebe ring. This enormous ring lies well outside the planet's co-rotating plasmasphere, and so plasma drag is probably not relevant for this ring, and indeed the inward drift of material observed in this system is consistent with a ring dominated by Poynting–Robertson drag (Verbiscer *et al.*, 2009; Tamayo *et al.*, 2011; Hamilton *et al.*, 2015; Tamayo *et al.*, 2016).

Turning to the various rings illustrated in Figure 12.11, the inward displacement of material in Jupiter's Gossamer rings and Uranus' μ ring suggest that $\mathcal{R}_F < 1$ for these rings, and so Poynting–Robertson drag dominates the semi-major axis evolution of these rings. Indeed, Burns *et al.* (1999) interpreted the structure of Jupiter's Gossamer rings in exactly these terms. However, the material in Saturn's G ring would appear to be spiraling outwards, indicating that plasma drag overwhelms Poynting–Robertson drag. Furthermore, while much of the E ring's radial extent appears to be associated with variations in the particles' orbital eccentricities rather than semi-major axis evolution (see below), detailed analysis shows that the semi-major axes of the E ring particles also tend to be displaced exterior to Enceladus' orbit (Hedman *et al.*, 2012). Thus it appears that $\mathcal{R}_F > 1$ for Saturn's dusty rings.

In order to evaluate whether it is reasonable for the Gossamer and μ rings to have $\mathcal{R}_F < 1$ and Saturn's G and E rings to have $\mathcal{R}_F > 1$, let us define the critical plasma ion mass density:

$$\rho_i^{crit} = \frac{3}{2} \frac{Q_{PR}}{\zeta} \left(\frac{1\text{AU}}{a_p} \right)^2 \frac{S_0}{c^2} \frac{1}{na(\Omega_p/n - 1)^2}, \tag{12.12}$$

which is the plasma mass density required for plasma drag to exactly balance Poynting–Robertson drag (i.e. to make $\mathcal{R}_F = 1$). If the co-rotating plasma's mass density exceeds this value,

then the particles should spiral outwards, and if the plasma ion density is below this value, then Poynting–Robertson drag will dominate and particles will spiral in towards the planet. Assuming Q_{PR} is of order unity, the critical plasma densities for Saturn's G and E rings are 12 and 2 amu cm^{-3}, respectively. The measured ion densities in these regions vary quite a bit, but are typically in the range of 10–100 ions cm^{-3}, with the dominant species being O^+ and O_2^+ (Elrod *et al.*, 2012; Persoon *et al.*, 2013). Thus for Saturn's dusty G and E rings, the plasma density is sufficiently high for plasma drag to cause particles to spiral outwards. By contrast (again assuming Q_{PR} is of order unity) the critical plasma densities are 460 and 54 amu cm^{-3} for Jupiter's two Gossamer rings and 51 amu cm^{-3} for Uranus' μ ring. These are all higher than the critical values for Saturn's rings, indicating that it will be more difficult for plasma drag to overpower Poynting–Robertson drag in these cases. Unfortunately, there are no direct measurements of the plasma densities in the vicinity of Uranus' μ ring, but the Voyager measurements at larger radii generally indicated plasma number densities of around 1 ion cm^{-3} (McNutt *et al.*, 1987; Selesnick and McNutt, 1987). Measurements of the Jovian magnetospheric plasma interior to the Galilean satellites are also limited, but some plasma measurements from the end of the Galileo mission suggest that interior to 5 Jovian radii (that is, 333 500 km), the plasma number density drops to around 1 ion cm^{-3} (Menietti *et al.*, 2005), so it does seem likely that the plasma density in the vicinity of the Gossamer rings is low enough for Poynting–Robertson drag to dominate the semi-major axis evolution of the ring particles.

12.3.1.2 The Vertical Thicknesses of Distant Dusty Rings

The semi-major axis evolution of fine particles not only influences the radial structure of the dusty outer rings, but can also affect the vertical structure of the ring material. For example, when Jupiter's Gossamer rings, Saturn's E ring, or Saturn's Phoebe ring are viewed from edge on, all are found to have finite vertical thicknesses (see Figure 12.12). Furthermore, despite the large differences in the overall size of these rings, their vertical morphologies are quite similar in that they seem to have a roughly uniform brightness within a certain distance of the ring-plane. In fact, the brightest parts of each ring are not found along the ring-plane but in two bands located equal distances above and below this plane (Burns *et al.*, 1999; Kurth *et al.*, 2006; Showalter *et al.*, 2008; Kempf *et al.*, 2008; Verbiscer *et al.*, 2009; Hedman *et al.*, 2012). This distinctive morphology indicates that most of the particles in each of these rings have similar inclinations but randomly distributed ascending nodes. Particles on inclined orbits move up and down as they orbit the planet, and since each particle's vertical velocity is zero near the extremes of their vertical motion, they will spend more time at those vertical locations, naturally enhancing the ring's brightness above and below the midplane.

For Jupiter's Gossamer rings and Saturn's Phoebe ring, the common inclination of the ring particles matches the inclination of the moon that is the most likely dominant source of the ring material. Jupiter's moons Amalthea and Thebe have inclinations that carry them ±1200 km and ±4200 km above and below Jupiter's equatorial plane, which corresponds to the

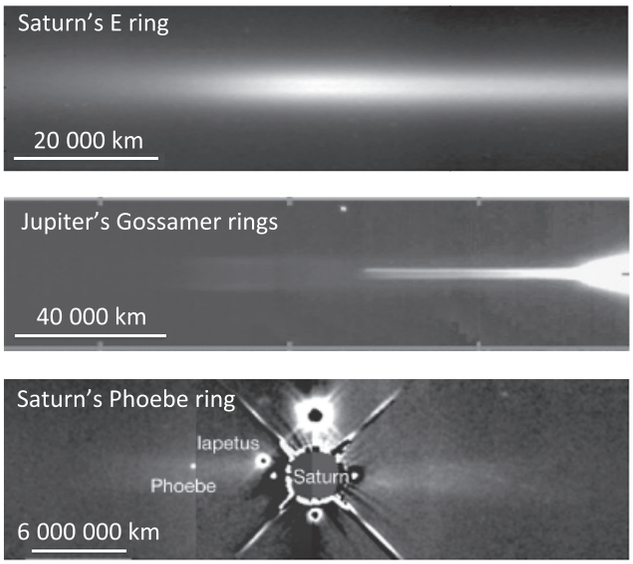

Figure 12.12 Edge-on views of several dusty rings. The top panel is an image of Saturn's E ring obtained by the Cassini spacecraft (modified from Planetary Photojournal Image PIA7803), the middle panel is of Jupiter's Gossamer ring as observed by the Galileo spacecraft (Showalter *et al.*, 2008), and the bottom panel is Saturn's Phoebe ring as viewed by the WISE satellite (Hamilton *et al.*, 2015). Note that all rings have a finite vertical thickness.

vertical thicknesses of the two Gossamer rings shown in Figure 12.12. Similarly, Phoebe has an inclination that carries it ±1 600 000 km from the planet's orbital plane (the relevant plane for this distant ring), which matches the vertical thickness of that enormous ring. While this reinforces the idea that these rings consist primarily of debris knocked from each of these moons, it also means that the material in these rings is not just following the inclined orbit of its parent moon. Instead, it appears that the particles in these rings all have about the same orbital inclinations as their source moon, but the ascending nodes of these orbits are evenly distributed around the planet.

The locations of the ring-particles' ascending nodes most likely have become dispersed around the planet thanks to differential nodal regression. Any object that is in orbit around a giant planet will have its ascending node slowly drift around the planet. For dust grains, non-gravitational forces can potentially influence this rate (see below), but even for large objects like moons, asymmetries in the planet's gravitational field due to its finite oblateness cause nodes to regress at a rate that depends upon the objects' semi-major axis (see Chapter 2). Hence, as the dust grains migrate inwards under the influence of drag forces, one expects that their nodal regression rates will have a range of values, allowing the node locations to become scattered all around the planet (Burns *et al.*, 1999).

The vertical structure of the E ring has a slightly different explanation. In this case, the inclination of its source moon is small compared with the ring's vertical thickness. However, the particles in this ring are all launched from Enceladus' south pole with a net southwards velocity. Furthermore, only particles traveling fast enough to escape the moon's gravity and avoid recollision with Enceladus can populate the E ring, so the material that forms the E ring must start off with a non-zero inclination. Indeed, numerical simulations show that these interactions

with Enceladus, perhaps moderated by additional electromagnetic perturbations to the particles' orbits, can reproduce this ring's finite vertical extent (Juhász *et al.*, 2007; Kempf *et al.*, 2010).

12.3.1.3 Aligning Orbits with Solar Radiation

Having examined how perturbation forces can change the semimajor axes and orientations of particles' orbits, we can now turn our attention to processes that alter orbital eccentricities and inclinations. The most efficient way to excite eccentricities and inclinations is to break the azimuthal symmetry of the planetary environment, and for many dusty rings the Sun is the most important source of such asymmetric forces. Most directly, solar radiation pressure pushes any object that can scatter or absorb photons away from the Sun. However, as we will discuss in the next subsection, solar radiation also influences the charge state of dust grains, so the electromagnetic forces experienced by material in dusty rings can change as they pass through the planet's shadow.

Probably the most straightforward examples of how solar radiation can affect the orbits of fine dust grains can be found not in the broad outer rings, but in a few of the narrow ringlets that lie within Saturn's main rings, specifically the dusty ringlets in the Encke Gap near the outer edge of Saturn's A ring and the so-called "Charming ringlet" in the Cassini Division's Laplace Gap (see Figure 12.13). These ringlets are non-circular and are typically found further from the planet's spin axis when they are observed on the sunward side of the planet than they are when observed near the planet's shadow (Hedman *et al.*, 2010b, 2013). This "heliotropic" behavior is most likely due to the orbital eccentricities induced by solar radiation pressure.

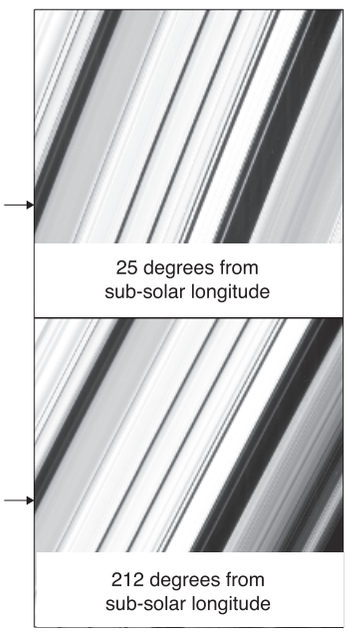

Figure 12.13 Example of a dusty ringlet whose shape is influenced by solar radiation pressure. The above images were obtained by Cassini in 2008 and have been separately cropped, rotated and stretched to facilitate comparisons. In both images, radius in the rings increases towards the upper left. The arrows point to the dusty "Charming ringlet" in the Laplace Gap. Note that this ringlet is found further from the planet (closer to the outer edge of the gap) at longitudes closer to the Sun (adapted from Hedman *et al.*, 2010b).

Solar radiation pressure is a perturbing force that acts in a nearly fixed orientation in inertial space, and so causes particles to slow down and speed up as they move around the planet towards and away from the Sun (see Chapter 2). These alternating accelerations will cause particles to follow orbits with eccentricities that either grow or shrink over time, depending on where their orbital pericenters are located relative to the Sun. In fact, since other phenomena like asymmetries in the planet's gravitational field will tend to cause a particle's orbital pericenter location to drift around the planet, the orbit's eccentricity will oscillate over time. However, for any combination of an inertially fixed force and a perturbation that causes eccentric orbits to steadily precess around the planet at a fixed rate $\dot{\varpi}_0$, there is one solution to the equations of motion that corresponds to an orbit with a constant eccentricity and a fixed pericenter location. For solar radiation pressure, the orientation of this fixed orbit is always along the Sun–planet line. If orbits tend to precess in the prograde direction relative to the Sun (i.e. $\dot{\varpi}_0 > n_s$, where n_s is the rate of the Sun's apparent motion around the planet), then this fixed orbit will have its apocenter aligned with the Sun, but if $\dot{\varpi}_0 < n_s$, this orbit will have its pericenter aligned with the Sun (Hamilton, 1996). Furthermore, so long as solar radiation pressure is a sufficiently weak perturbation and the orbital precession rate is sufficiently fast, the eccentricity of this fixed orbit is given by the following formula:

$$e_f \simeq \frac{9}{8}\frac{S/c}{GM_P}\cos B \frac{n}{|\dot{\varpi}_0|}a^2\frac{Q_{PR}}{\rho r_g}, \tag{12.13}$$

where S is the solar radiation flux, c is the speed of light, M_P is the planet's mass, B is the elevation angle of the Sun above the ring-plane, Q_{PR} is the Poynting–Robertson efficiency factor, and ρ and r_g are the particle's mean density and radius. Note that this forced eccentricity is inversely proportional to the particle's size, which simply reflects the fact that smaller particles are more easily perturbed by non-gravitational processes.

The observed variations in the location of the "heliotropic" dusty ringlets are perfectly consistent with these sorts of orbital perturbations. The fact that the ringlets are found further from the planet near sub-solar longitudes indicates that the material in these ringlets have their orbital apocenters aligned with the Sun, which is consistent with Saturn's oblateness dominating the particles' apsidal precession rates. Furthermore, the observed variations in the ringlets' radial positions indicate that the typical orbital eccentricities induced by the Sun are about 0.000 035 for the Encke Gap ringlets and 0.000 14 for the Charming ringlet (Hedman *et al.*, 2010b, 2013). Such values of e_f are consistent with ice-rich particles with radii of several tens of microns.

12.3.1.4 Dispersing Material with Sunlight and Other Forces

When coupled with other forces, solar radiation pressure can not only distort the shapes of narrow ringlets, but can also disperse material over a wide range of radii. Indeed, just such an interplay of perturbing forces is thought to be responsible for aspects of the radial structure of Jupiter's Thebe ring, Saturn's Phoebe ring, and, especially, the E Ring.

While most of the material in both Jupiter's Thebe ring and Saturn's Phoebe ring extend radially inward from their source satellites (see Figure 12.11), they each also have faint outward extensions. As discussed above, the inward flow of material arises from Poynting–Robertson drag forces, which cause grains to slowly spiral in toward their planets. The exterior components, however, require other explanations. Two main possibilities exist: (i) a mechanism to increase particle eccentricities so that orbital apocenters can extend beyond the source satellite, and (ii) additional and more distant source bodies.

Radiation pressure on small Phoebe ring dust grains drive up orbital eccentricities so that they can extend well beyond the orbit of Phoebe (Hamilton *et al.*, 2015; Tamayo *et al.*, 2016). In addition, a population of distant satellites an order of magnitude smaller than Phoebe itself are also likely contributors to the giant ring (Hamilton *et al.*, 2015; Tamayo *et al.*, 2016). Crucially, several of these satellites share Phoebe's orbital inclination, allowing their debris, large and small, to spread over the same vertical thickness as Phoebe material. Other distant satellites, while more numerous, all have much more highly tilted orbits, so that their debris forms a vertically extended thick diffuse background that is likely not detectable with current instruments (Hamilton *et al.*, 2015). Which of these two explanations is most important in the Phoebe ring remains an open question.

For the Thebe ring extension, there are no known moons between Thebe's and Io's orbits, and radiation pressure is too weak to force eccentricities as large as would be needed to produce the observed extension. Instead, electromagnetic forces arising from the motions of ring particles through Jupiter's intense magnetic field are likely responsible for driving radial motions. The electric charges on dust grains vary periodically when their orbits bring them into Jupiter's shadow (Horányi and Burns, 1991). Detailed calculations show that the changing charges on small grains, and the resulting periodic modulations in the non-gravitational forces can indeed enable particles launched from Thebe to reach ∼40 000 km beyond Thebe's orbit, in agreement with observations (Hamilton and Krüger, 2008). Similar processes also drive even tinier grains to ∼20° inclination, accounting for this population of grains observed by Galileo's dust detector during its final few orbits around Jupiter (Krüger *et al.*, 2009; Hamilton and Krüger, 2008). Interestingly, the Amalthea Gossamer ring does not show a similar outward extension, possibly because Amalthea is located just exterior to synchronous orbit where velocities relative to Jupiter's spinning magnetic field are low and electromagnetic forces correspondingly weak (Hamilton and Krüger, 2008).

Unlike the other diffuse rings shown in Figure 12.11, the E ring extends a substantial distance both interior and exterior to the orbit of its source moon Enceladus. Indeed, *in situ* measurements reveal that E ring particles can be found over a very broad region all the way out to the orbit of Titan (see Figure 12.14). In part, the radial extent of this ring can be attributed to plasma drag, which is quite effective for the small E ring grains (Morfill and Gruen, 1979; Morfill *et al.*, 1993; Dikarev, 1999; Srama *et al.*, 2011). However, many aspects of the E ring's structure can be most easily explained if the particles in this ring have substantial orbital eccentricities, enabling them to wander over a substantial radial range as they orbit the planet.

It has long been suspected that the micron-sized E ring particles are particularly susceptible to having their eccentricities excited by an interaction between electromagnetic and solar radiation forces (Horányi *et al.*, 1992; Hamilton, 1993; Hamilton and Burns, 1994). The basic idea is that when the small particles in this ring become charged due to their interactions with the surrounding plasma and the ionizing radiation from the Sun, they experience a Lorentz force from Saturn's magnetic field that tends to counteract the apsidal precession induced by the planet's gravitational field. In fact, for micron-sized particles these two forces can nearly cancel each other out, greatly reducing the apsidal precession rate $|\dot{\varpi}_0|$. This, together with the small grain size, enables solar radiation pressure to excite exceptionally large eccentricities in the particle's orbits (i.e. the forced eccentricity e_f of Equation (12.13) can become large).

This basic picture has been expanded upon with increasingly detailed analytical and numerical calculations, including not only solar radiation pressure and plasma interactions, but also processes like sputtering, which gradually reduces the size

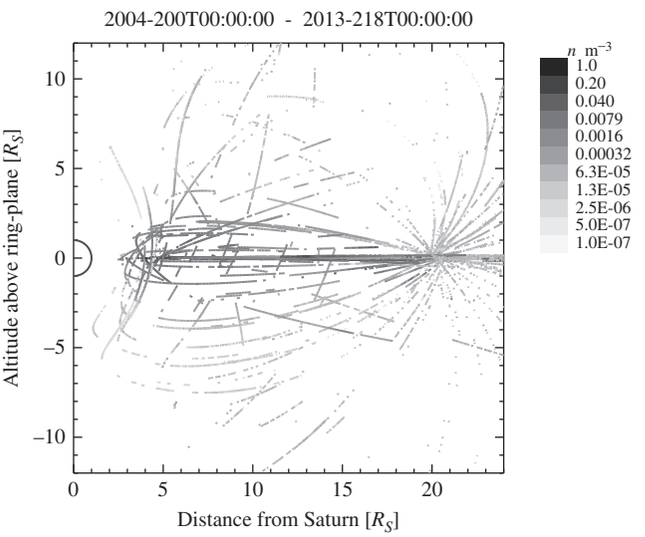

Figure 12.14 The apparent dust density (in particles per cubic meter) measured by the CDA instrument between 2004 and 2014 along the Cassini trajectory in a Saturn-centered coordinate system in an edge-on view to the ring-plane. The trajectory of Cassini is easily recognizable. Blank areas along the track represent periods where the CDA was not able to record meaningful data. (These are primarily caused by long periods of inadequate pointing of Cassini where the dust RAM direction was not in the field-of-view of the CDA.) Adapted from Srama *et al.* (2011).

of the E ring grains (Jurac *et al.*, 2001; Juhász and Horányi, 2004; Juhász *et al.*, 2007; Horányi *et al.*, 2008). At the same time, Cassini measurements are now able to confirm important aspects of these theoretical models. For example, CDA measurements show that E ring grains located within 42 000 km of Saturn are charged to a few volts negative potential, while grains located further out are charged positively (Kempf *et al.*, 2006). This charge state is consistent with the variations in the local plasma environment (Arridge *et al.*, 2011), and the negative charge of the central E ring is sufficient to significantly influence the apsidal precession rate of micron-sized ice grains. Meanwhile, both remote-sensing and *in situ* measurements reveal that early in the Cassini mission, during Saturn's northern winter, the E ring was warped into a shallow cone with the densest part of the ring falling north of Saturn's equator plane at large radii and south of that plane closer to the planet (Nicholson *et al.*, 1996; de Pater *et al.*, 2004; Kempf *et al.*, 2008; Hedman *et al.*, 2012; Ye *et al.*, 2016). This aspect of the E ring's structure was actually predicted theoretically by the above models (Hamilton, 1993), where it arises because solar-radiation pressure has a northwards component during this time. Since the particles on eccentric orbits spend more time further from Saturn, this vertical component of solar radiation naturally drives the apocenter of the ring particles' orbit northwards, which also pulls the pericenter southwards. Indeed, the observed average warp in the ring is quite consistent with theoretical predictions based on this model (Hamilton, 1993; Hedman *et al.*, 2012). Furthermore, since this aspect of the E ring's structure should change with Saturn's season as the Sun moves from south to north, future analysis of Cassini data should provide more stringent tests of these models.

At the same time, there are other aspects of the E ring's structure that were not predicted by the theoretical calculations and are still mysterious. For example, observations from early in the Cassini mission reveal that the E ring's brightness and density vary systematically with longitude relative to the Sun (Hedman *et al.* 2012; Kempf *et al.*, in preparation). Some of these variations can be attributed to orbital alignments associated with solar radiation pressure and charge variations associated with passage through Saturn's shadow. However, even after accounting for these variations, it appears that the ring is systematically brighter at longitudes closer to the Sun. While the orientation of this asymmetry strongly suggests that solar radiation forces are involved, other asymmetries in the Saturn system like the noon-to-midnight electric field (Andriopoulou *et al.*, 2012, 2014; Wilson *et al.*, 2013) could also be relevant. At the moment, no theoretical model has been able to produce this sort of asymmetry, and additional observational data, as well as new theoretical calculations, will likely be needed to clarify what is happening.

12.3.2 Disturbing Dusty Rings with Impulsive Events

While many features of dusty rings can be attributed to steady perturbing forces, there are some structures that seem to be due to specific events in the ring's recent history. In particular, both Jupiter's Main ring and Saturn's D ring contain periodic brightness variations (see Figure 12.15). In Jupiter's ring, the intensity

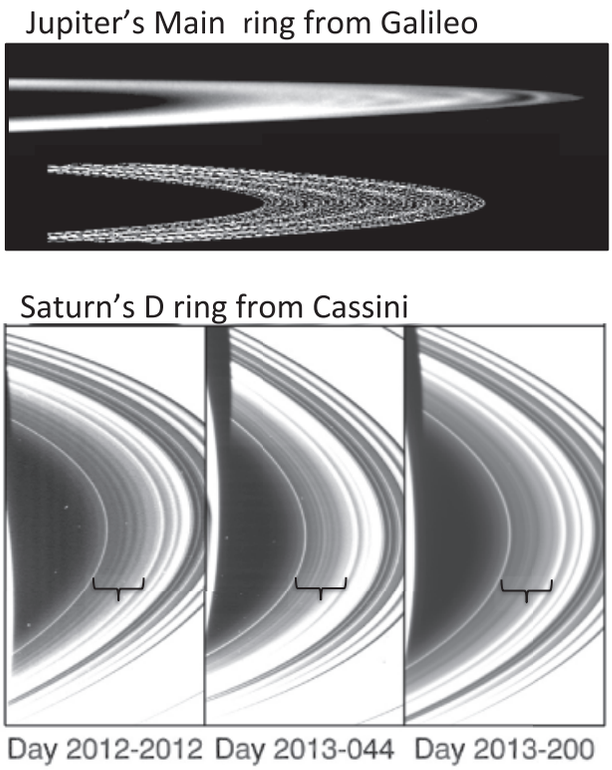

Figure 12.15 Structures in dusty rings created by impulsive events. The upper panel shows a nearly edge-on view of Jupiter's Main ring from the Galileo spacecraft that shows bright and dark patches that likely represent a corrugation in the rings illustrated with the wire mesh model (Showalter *et al.*, 2011). The lower panel shows images of Saturn's D ring obtained by the Cassini spacecraft which show periodic brightness variations in the region marked with the brackets (Hedman and Showalter, 2016). The wavelengths of both these patterns steadily decrease over time.

of this brightness variation varies with longitude in a manner consistent with a vertical corrugation (Showalter *et al.*, 2011). In Saturn's D ring, some of the periodic structures also appear to be corrugations, while others seem to represent real variations in the rings' local surface density (Hedman *et al.*, 2007a, 2011a, 2015; Hedman and Showalter, 2016). However, what makes all of these structures remarkable is that their wavelengths are observed to decrease over time in a very predictable way. This evolution in the pattern's wavelength can be explained with a simple model, in which some event suddenly imparts some vertical and/or horizontal momentum to the ring particles, causing them to all follow inclined and/or eccentric orbits with initially aligned nodes and/or pericenters, creating a ring with a slight tilt and/or offset. The ring, however, cannot remain in this simple configuration because it consists of particles with a range of semi-major axes, and so the locations of the nodes and pericenters will drift around the planet at different rates, causing any tilt in the ring to wind up into a corrugation, or any offset to wind up into a spiral pattern (see Figure 12.16). Furthermore, the wavelengths of these patterns will get smaller over time as the spiral becomes increasingly tightly wound. The winding rate is determined by the planet's gravitational field, and to first order the pattern's radial wavenumber ($k = 2\pi/\lambda$, where

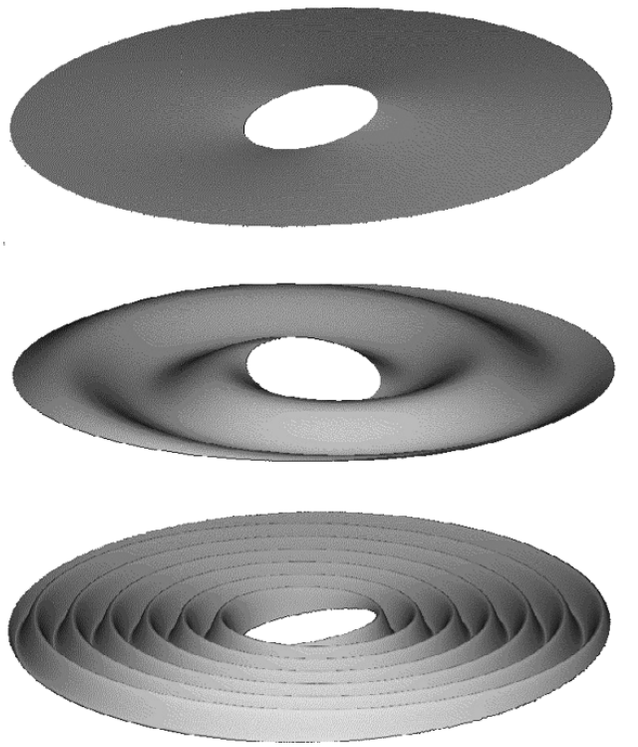

Figure 12.16 Cartoon illustrating how an initially tilted ring can transform into a corrugated ring due to differential nodal regression. For the sake of clarity we have omitted the central planet in all these images. The top image shows a tilted ring where all the ring-particle's orbits have comparable inclinations and ascending nodes at the same longitude. Over time, the node positions drift around the planet at different rates, transforming the tilted ring into a corrugated ring.

λ is the pattern's wavelength) should be given by the following expression:

$$k = \frac{21}{4} J_2 \sqrt{\frac{GM_P}{r^5}} \left(\frac{R_P}{r}\right)^2 \delta t, \tag{12.14}$$

where r is the ring radius, M_P and R_P are the planet's mass and radius, J_2 is a standard measure of the planet's oblateness, and δt is the amount of time that has elapsed since the ring was disturbed. The observed trends in the wavelengths of the patterns in both Jupiter's and Saturn's rings follow this prediction remarkably well, and so it is reasonable to conclude that these structures are due to ring-disturbing events that occurred in the recent past.

The nature of these ring-disturbing events can be further explored by extrapolating the observed trends in the pattern's wavelength back in time and thereby estimating when the event occurred. For example, analyses of the corrugation in Jupiter's rings revealed that this ring became tilted during the summer of 1994, when debris from the comet Shoemaker-Levy 9 was crashing into Jupiter (Showalter *et al.*, 2011). Thus it is reasonable to conclude that Jupiter's ring became tilted due to cometary debris crashing into the ring particles. These patterns can therefore provide records of past impact events. Indeed, one set of patterns in Saturn's rings appears to have formed around 1983, and may represent another impact event (Hedman *et al.*, 2011a, 2015). In this case, we have no direct observation of the impact, but the fact that both the dusty D ring and the dense C ring were affected makes it the most likely option. This would mean that the rings can preserve records of impacts for decades after they occur. More recently, another pattern was found in the D ring that appears to have formed in late 2011 (Hedman and Showalter, 2016). In this case, the origin of the disturbance is less clear. It could be another impact, but it could also reflect a rapid shift in the state of Saturn's electromagnetic environment. Future analyses of contemporary Cassini *in-situ* measurements of Saturn's magnetosphere will hopefully help constrain these possibilities.

12.3.3 Resonant Structures in Faint Rings

In addition to steady forces and impulsive events, dusty ring material can also be sculpted by periodic perturbing forces due to various moons and magnetospheric asymmetries. These time-variable forces on the ring particles produce a wide variety of dramatic structures in both dense and dusty rings at locations where the orbital period of the ring particles is approximately a whole number ratio times the orbital period of the perturbing force. For dusty rings, the best-studied structures produced by these sorts of resonances are the longitudinally confined arcs in both Neptune's Adams ring and several of Saturn's narrower distant rings. However, resonant phenomena also play a role in the vertical structure of Jupiter's Halo ring and appear to organize material in Saturn's D ring, Roche Division, and spokes.

12.3.3.1 A Brief Review of Important Mean-Motion Resonances

Resonances occur when the frequency of a periodic perturbing force acting on the ring particles is close to a whole number ratio times the particles' orbital frequencies. In these situations, small perturbing forces can build up and have significant effects on the particles' orbital parameters (see Chapter 2). However, there are a number of different types of resonances that influence different orbital parameters. The resonances we will consider in this section are as follows.

- **Lindblad (eccentric) resonances (LER)**, which affect the ring-particles' orbital eccentricities. These resonances occur at radial locations where the difference between the angular frequency of the perturbing potential ω_p and the ring-material's orbital mean motion n is an integer m times the ring-materials' radial epicyclic frequency $\kappa = n - \dot{\varpi}_0$, where $\dot{\varpi}_0$ is the apsidal precession rate:

$$\kappa = m(n - \omega_p). \tag{12.15}$$

  When the perturbing force is the gravitational pull of a satellite, the strongest such resonances occur at the locations where ω_p equals the satellite's mean motion n_S, and so the resonant condition becomes:

$$\kappa = m(n - n_S), \tag{12.16}$$

  where $n - n_S$ is the synodic frequency at which the satellite comes into conjunction with the particle. This expression can also be written in the following form:

$$mn_S = (m - 1)n + \dot{\varpi}_0. \tag{12.17}$$

- **Vertical (inclination) resonances (VIR)**, which affect the ring-particles' orbital inclinations. These occur where the difference between the angular frequency of the perturbing potential ω_p (which must now produce a vertical force) and the ring-material's orbital mean motion n is an integral multiple of the ring-materials' vertical epicyclic frequency $\nu = n - \dot{\Omega}_0$, where $\dot{\Omega}_0$ is the nodal regression rate:

$$\nu = m(n - \omega_p). \tag{12.18}$$

  If the perturbation is due to the gravity of a vertically inclined satellite with mean motion n_S and nodal regression rate $\dot{\Omega}_S$, then the strongest resonances occur where

$$mn_S = (m-2)n + \dot{\Omega}_0 + \dot{\Omega}_S. \tag{12.19}$$

  Note that this differs somewhat from the condition for the strongest Lindblad resonances because it is the motion of the ring-particles' node relative to the moon's node that determines the period of the vertical force.
- **Co-rotation (eccentric or inclination) resonances (CER/CIR)**, which affect the ring-particles' semi-major axes and can confine material in longitude. The most powerful examples of these resonances occur when the ring-material has almost the same mean motion as a satellite, in which case the perturbations from the co-orbiting moon can cause material to librate around the moon's Lagrange points. However, if the moon is on an eccentric or inclined orbit, co-rotation resonances can occur at multiple semi-major axes. For example, if a satellite is on an eccentric orbit with a mean motion n_S and an apsidal precession rate $\dot{\varpi}_S$, then co-rotation eccentricity resonances can occur where

$$mn_S = (m-1)n + \dot{\varpi}_S. \tag{12.20}$$

Note that the conditions for all three types of resonances with satellites occur where $mn_S \simeq (m-1)n$ (technically, the corresponding vertical resonances have $2mn_S \simeq (2m-2)n$), so it is possible for multiple resonances to influence the ring-particles' orbital properties at once. Indeed, for $m >> 1$, each co-rotation eccentricity resonance is situated very near a corresponding Lindblad resonance with the same satellite. Comparing Equations (12.20) and (12.17) reveals that the mean motions of the two resonant locations differ by:

$$\delta n = n_{CER} - n_{LER} = \frac{\dot{\varpi}_0 - \dot{\varpi}_S}{m-1}. \tag{12.21}$$

Both of the above precession rates are set by the planet's gravitational field, so the physical separation between these two resonances can be written as:

$$a_{LER} - a_{CER} \simeq \frac{2}{3} a \frac{\delta n}{n} \propto J_2 \left(\frac{R_P}{a}\right)^2 a\mathcal{F}(m), \tag{12.22}$$

where R_P and J_2 are the radius and the oblateness of the central planet, while $\mathcal{F}(m)$ is a positive number that depends on m. Note that since δn is always strictly positive when the ring material is interior to the moon, in these cases the CER is always closer to the planet than the LER. Such interacting resonances probably play an important role in the formation of longitudinally confined ring arcs. Because of these complications, we will consider those systems after first discussing some simpler patterns that appear to be generated by the action of individual resonances. Some of these are also due to resonances with the planet's various moons, but others can be attributed to resonances with asymmetries in the planet's electromagnetic field.

12.3.3.2 Vertically Extended Dusty Rings Produced by Vertical Resonances

Jupiter probably provides the clearest example of how resonances with a planet's electromagnetic field can influence the structure of a dusty ring. Jupiter, of course, has a very powerful magnetic field that is tilted by roughly 10° from the planet's spin axis, so Jupiter's rotation produces clear time variations in the planet's magnetic field and radio emissions, allowing the planet's rotation period to be precisely measured. Hence the relevant perturbation frequency is well known and it is relatively straightforward to determine the locations in Jupiter's rings where various resonances with the magnetic field might exist. In particular, it turns out that the transition between Jupiter's flat Main ring and its vertically extended Halo ring occurs close to the 3 : 2 "Lorentz" resonance with the planet's magnetic field (Burns *et al.*, 1985). At these resonances, governed by an equation like Equation (12.19) but with n_S reinterpreted as the planet's spin rate, the periodic vertical forces from the rotating magnetic field become commensurate with the particles' epicyclic vertical frequency, which allows those perturbations to excite significant inclinations (Hamilton, 1994). Indeed, it is thought that the Halo ring consists of material derived from Jupiter's Main rings that has slowly drifted inwards under the influence of Poynting–Robertson drag until it passed through these Lorentz resonances to become vertically puffed up into the Halo ring (Burns *et al.*, 1985).

12.3.3.3 Patterns Generated in Dusty Rings by Lindblad Resonances

Cassini observations have revealed several structures in dusty rings that are probably generated by Lindblad resonances. The most straightforward example of these is a series of dark gashes in the outer part of Saturn's G ring, around 170 000 km from Saturn's center (see the lower panel of Figure 12.17). These gashes fall on top of the 8 : 7 Lindblad resonance with Mimas, and they probably arise because the particles near this resonance are having their orbital eccentricities excited and aligned by Mimas' gravitational perturbations. In dense rings, these organized motions give rise to sharp edges or spiral density waves (see Chapters 3, 10, and 11) that track the moon that generated them, and these gashes seem to be the analogous structures for faint rings. Indeed, these patterns can be reproduced using a relatively simple model where the particles' average orbital eccentricity and pericenter locations follow prescribed trends in the vicinity of the resonance (Hedman *et al.*, 2009b).

Similar patterns of diagonal dark bands can also be found in the Roche Division and D ring (Hedman *et al.*, 2009b). In these cases, there is no Lindblad resonance with any known satellite that could produce these features. However, these features do occupy regions where the mean motions of the ring particles are 4/3 and 1/2 of the planet's rotation rate, respectively. Thus these

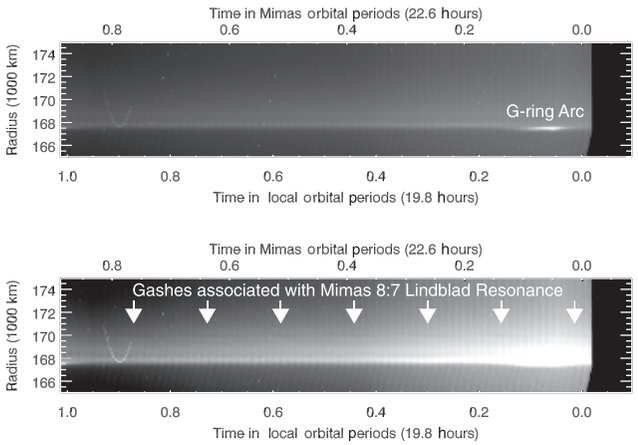

Figure 12.17 Maps of Saturn's G ring derived from Cassini images, each showing the brightness of the ring at a particular inertial longitude as a function of radius and time (a proxy for co-rotating longitude). In the upper panel, the most obvious feature is a longitudinally confined arc of material around 167 500 km, which is likely confined by the 7 : 6 co-rotation eccentricity resonance with Mimas. In the contrast-enhanced lower panel a series of dark gashes can be seen in the ring around 170 000 km, which are probably generated by the 8 : 7 Lindblad resonance with Mimas (from Hedman *et al.*, 2009b).

patterns are probably generated by Lindblad resonances with asymmetries in the planet's gravitational or electromagnetic fields. Indeed, some of these patterns were observed to track variations in the planet's radio emissions, supporting the notion that they are driven by non-gravitational perturbing forces.

12.3.3.4 Resonances and the Formation of Spokes

The formation of the dusty "spokes" that appear over Saturn's B ring near the planet's synchronous orbit may also involve resonant phenomena. Some of these features have narrow radial morphologies, while others are triangular with an apex pointing toward the location of the synchronous orbit (i.e. where $n = \Omega_p$). Some of the triangular structures have sharp radial edges, while others appear to be older and sheared out by the Kepler motion of the individual ring particles. Radial edges, proximity to synchronous orbit, and the pointing of triangular spokes all strongly suggest the importance of electromagnetic forces. Imaging studies with Voyager, Hubble, and Cassini data all indicate that spokes are composed of micron-sized dust grains (Doyle and Grun, 1990; McGhee *et al.*, 2005; Mitchell *et al.*, 2013). As previously described in Section 12.2.1.1, Cassini infrared imaging indicates that somewhat larger dust grains are also present in spokes (D'Aversa *et al.*, 2010).

Spokes were plentiful in Saturn's rings during the Voyager era when Saturn was near equinox and the rings were nearly edge-on as seen from the Earth and Sun. As Saturn progressed toward solstice, however, the rings opened up to present a more face-on aspect to the Earth. Long-term monitoring from the Hubble Space Telescope revealed that spokes gradually disappeared during this time (McGhee *et al.*, 2005), reappearing only many years later after Cassini's arrival at Saturn (Mitchell *et al.*, 2013).

Both Voyager and Cassini imaging show that spokes can form anywhere in the B ring, but that they display a marked preference for the morning side of the ring and for particular phases of the planet's periodically modulated radio emissions (Porco and Danielson, 1982; Mitchell *et al.*, 2013). These findings suggest that asymmetries in Saturn's electromagnetic field play some role in generating or controlling these features. However, while the Cassini data has confirmed that spoke periodicities are close to the periodicities in the magnetosphere, the connection with the specific time-variable periods is still unclear. Most theories for spokes rely on meteoroid impacts into the ring to trigger spoke formation (Goertz and Morfill, 1983), and such impacts have been observed both indirectly (Hedman *et al.*, 2011a) and directly (Tiscareno *et al.*, 2013) in the Cassini era. Some have even suggested that spokes are formed by storms in Saturn's atmosphere that perturb the electromagnetic environment over the rings (Jones *et al.*, 2006). It is fair to say that, 35 years after their discovery, spokes remain a mystery.

12.3.3.5 Co-rotation Resonances, Saturn's Tenuous Ring Arcs, and Embedded Moons

Longitudinally confined ring arcs have been observed in the dusty rings around both Neptune and Saturn. Around Neptune, four arcs (named Courage, Liberté, Egalité, Fraternité) are confined in a 40-degree-wide azimuthal range within the Adams ring (Smith *et al.* 1989; see Figure 12.18). These incomplete rings have maintained their basic structure since their discovery in 1984 (Hubbard *et al.*, 1986) although adaptive-optics images obtained between 2002 and 2007 with the Keck and the VLT telescopes showed significant changes in the brightness of these arcs, with the leading two arcs almost disappearing in more recent data (de Pater *et al.*, 2005; Renner *et al.*, 2014). More recently, data from the Cassini spacecraft have revealed much more tenuous arcs of material surrounding the tiny moons Aegaeon, near the inner edge of the G ring (see upper panel of Figure 12.17), and Anthe and Methone (Figure 2.18). Again, these arcs of debris appear to be stable for multiple years.

Persistent ring arcs require some active confinement mechanism because an unconfined arc of particles following Keplerian orbits with average semi-major axis a and average mean motion n will have a spread of mean motions δn given by the following expression:

$$\delta n = -\frac{3}{2} n \frac{\delta a}{a}, \tag{12.23}$$

where δa is the spread in the semi-major axes. The corresponding spreading timescale is:

$$T_S = \frac{2\pi}{|\delta n|} = \frac{4\pi}{3\sqrt{GM_P}} \frac{a^{5/2}}{\delta a}, \tag{12.24}$$

where M_P is the mass of the central planet. This timescale is very short for the known arcs. For example, Neptune's ring arcs would be spread into complete rings over a timescale $T_S \simeq 3.4$ yr, using $a = 62\,932.7$ km (Renner *et al.*, 2014), $GM_P = 6.8351 \times 10^6$ km^3 . s^{-2} (Owen *et al.*, 1991), and assuming that the radial width of the arcs, $W \simeq 15$ km (Porco *et al.*, 1995), is equal to the semi-major axis dispersion δa. Alternatively, these

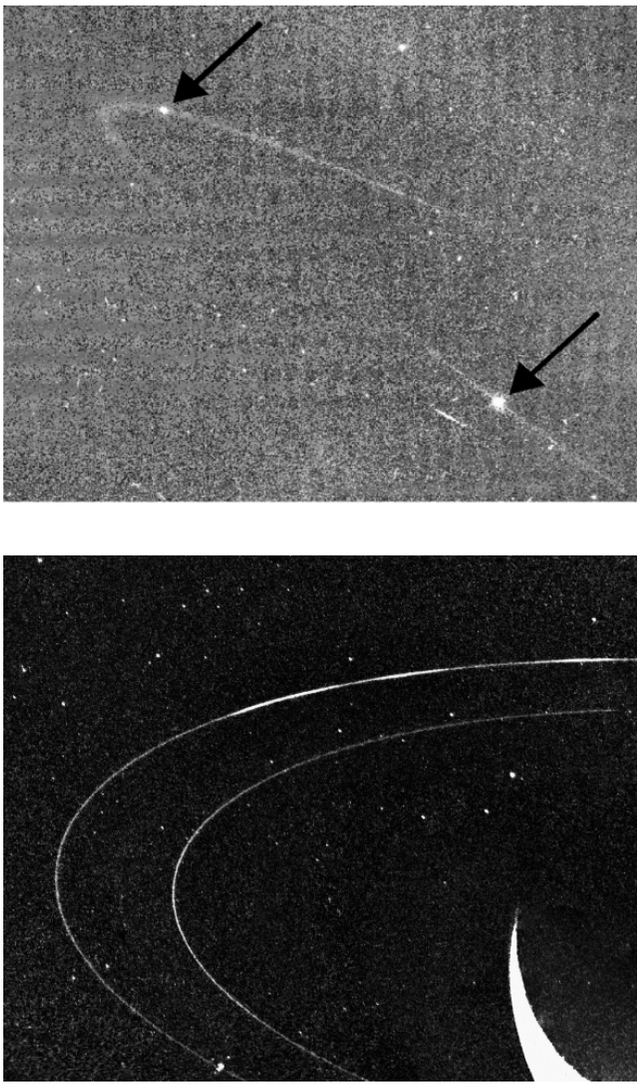

Figure 12.18 Images of arcs in dusty rings. The top image from the Cassini spacecraft shows faint arcs of material orbiting Saturn that are associated with the small moons Anthe and Methone (Planetary Photojournal image PIA11102). The bottom image from the Voyager spacecraft shows the arcs in Neptune's Adams ring (Planetary Photojournal image PIA01493).

arcs should lengthen at a rate of about 0.3 deg . day^{-1}. Such a large value should have been detected by the observations, but were not, thus showing that the arcs are actively confined.

Co-rotation resonances provide a natural mechanism for confining ring material in radius and longitude because in the restricted three-body problem a ring particle can remain trapped within a finite range of longitudes in any reference frame rotating at a mean motion n that satisfies Equation (12.20) for co-rotation eccentricity resonances or a similar expression for co-rotation inclination resonances. Indeed, such resonances have been invoked to explain both Saturn's and Neptune's ring arcs.

Even though they were found later, we will consider Saturn's ring arcs first because their confinement is somewhat easier to understand. The average mean motions of these arcs match those expected for material confined by Co-rotation Eccentricity Resonances (CERs) with Mimas, with the G ring arc occupying the 7:6 CER and the material associated with Anthe and Methone being trapped within the 10:11 and 14:15 CERs, respectively (Hedman *et al.*, 2009a, 2010a). Furthermore, these resonances clearly influence the motion of the arcs' source moons, and indeed Aegaeon, Methone, and Anthe all appear to be trapped in the same resonances that confine the arcs (Spitale *et al.*, 2006; Cooper *et al.*, 2008). The material trapped in each arc can therefore be regarded as debris knocked off each moon with insufficient speed to escape the relevant co-rotation site. Furthermore, the optical depths of Saturn's ring arcs are very low ($<10^{-5}$), so collisions among the ring particles should be rare and we can model the arcs as a collection of test particles moving in the combined potential of Saturn and Mimas.

Even in these relatively simple situations, some important complications arise because Mimas' eccentricity is large enough (~ 0.02) for the CER libration sites to encompass the radial locations of the nearby Lindblad resonance. El Moutamid *et al.* (2014) developed a generic, dimensionless model to investigate the interactions between the m+1:m CER and Lindblad resonance. They studied the coupled effects of the two resonances through a two degrees of freedom system, for which a possible form of the equations of motion is[2]

$$\begin{cases} \dot{\chi} = & -\varepsilon_C \sin(\Psi_C) - \dot{J}_L \\ \dot{\Psi}_C = & \chi \\ \dot{h} = & -(\chi + D)k \\ \dot{k} = & +(\chi + D)h + \varepsilon_L, \end{cases} \tag{12.25}$$

where

$$\begin{cases} h = & \sqrt{3}|m|e\cos\Psi_L \\ k = & \sqrt{3}|m|e\sin\Psi_L \\ \Psi_C = & (m+1)\lambda_S - m\lambda - \varpi_S \\ \Psi_L = & (m+1)\lambda_S - m\lambda - \varpi \\ J_L = & 3m^2e^2/2 \\ \chi = & 3m(a - a_C)/2a_C \\ D = & (\dot{\varpi}_S - \dot{\varpi})/n_C \\ \varepsilon_L = & \sqrt{3}|m|A^m(M_S/M)(a/a_S) \\ \varepsilon_C = & 3m^2E^m e_S(M_S/M)(a/a_S). \end{cases} \tag{12.26}$$

The first two equations of the system (12.25) describe the CER and the last two describe the Lindblad resonance. Here Ψ_C and Ψ_L are the arguments of the CER and Lindblad resonance, respectively. The terms A^m and E^m are combinations of Laplace coefficients (Shu, 1984), which can be approximated by $A^m \sim -E^m \sim 0.8m$ for $|m| >> 1$. Note that χ measures the particle's distance from the CER, a_C is the CER radius, n_C the associated mean motion, and the three fundamental parameters of the model D, ε_L, ε_C are respectively the (normalized) distance in frequency between the CER and the Lindblad resonance, the eccentricity forcing by the Lindblad resonance, and the CER strength ($n\sqrt{|\varepsilon_C|}$ is the CER frequency). The coupling between the two resonances arises from the $\dot{J}_L$ term in the first equation and the χ term in the third and fourth equations. These

[2] Note that the dots in Equations (12.25) are the derivatives with respect to $n_C t$ where t is the usual time and n_C is the mean motion at the CER.

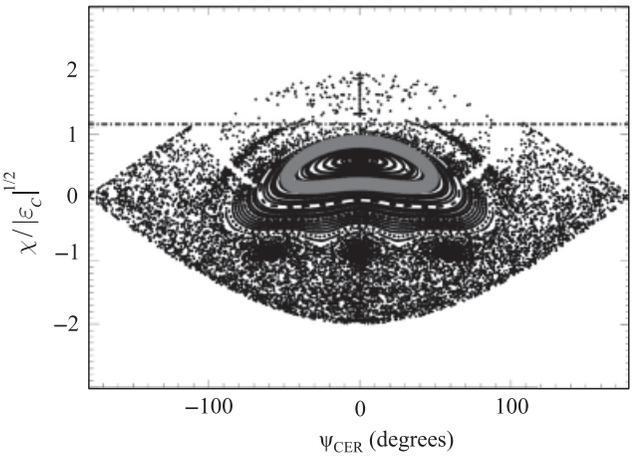

Figure 12.19 Surfaces of section for the parameters Ψ_C and χ (χ being measured in units of $\sqrt{|\epsilon_C|}$) in the vicinity of Aegaeon's orbit. The dashed-dotted horizontal line is the 7:6 LER radial location at $\chi = -D$. The gray curve corresponds to the actual orbit for Aegaeon, while the other surfaces of section correspond to particles having the same parameters as Aegaeon, except for the initial semi-major axis or χ (Equations (12.26)). The integration time is 830 years, and the initial is epoch 2004 October 08 06:01:00.5. (Adapted from EL Moutamid *et al*., 2014).

interactions can lead to chaotic motions in the vicinity of these resonances.

The large eccentricity of Mimas results in a strong coupling between the two resonances, causing the regular orbits of Anthe, Methone, and Aegaeon to be surrounded by large chaotic seas (El Moutamid *et al.*, 2014).[3] The chaotic regions are always surrounded by regular trajectories, so the CER stability is not affected. The equations can be numerically integrated to produce Poincaré surfaces of section (Ψ_C, χ). Figure 12.19 shows an example of this sort of plot for Aegaeon's motion in the 7 : 6 resonances. The position of the satellite (in gray) with respect to the CER radial location ($\chi = 0$) is plotted every time the k-component of the eccentricity vector is zero. The satellite initial conditions, the CER radius $a_C = 167491.6$ km, and the mass of Mimas are used to compute the parameters in Equations (12.26). The Lindblad resonance radius at $\chi = -D$ is indicated by a dashed-dotted horizontal line. In parallel to this work, an investigation of the long-term dynamical evolution (Callegari and Yokohama, 2010) found chaotic motions for objects on orbits close to Anthe's and Methone's that could lead to orbit crossings with Mimas in timescales of thousands of years.

It is also interesting to note that the semi-major axis variations for Aegaeon, ±4 km (Hedman *et al.*, 2009a, 2010a), are small with respect to the width of the co-rotation site (∼ 30 km). The satellites Anthe and Methone, located outside the orbit of Mimas (resonances 10:11 and 14:15, respectively), have similar surfaces of section (El Moutamid *et al.*, 2014), but with larger libration amplitudes in terms of semi-major axis, ±25 and ±20 km, respectively, i.e. about half of their CER widths (∼50 km). This is consistent with previous work that indicated Aegaeon's orbit is closer to the exact CER than Anthe's or Methone's are (Hedman *et al.*, 2010a). One possible explanation for this observation is that Aegaeon has undergone more significant orbital evolution via its interactions with the other objects in its arc. This would be consistent with the fact that Aegaeon's mass is much smaller relative to the total mass in its arc than Anthe's and Methone's masses are, but more detailed numerical calculations that consider interactions among multiple bodies in the resonance (cf. Sun *et al*., 2017) are needed to test this idea.

[3] By contrast, for Neptune's ring arcs, the Lindblad resonance is far enough from the CER and can therefore ensure the radial confinement of the collisional Adams ring (Goldreich *et al.*, 1986).

12.3.3.6 Neptune's Denser Ring Arcs, Confinement by Resonances and/or Co-orbital Moons

The dynamics of the arcs in Neptune's Adams ring are more complex than those of Saturn's tenuous ring arcs (see Chapter 5). This may be because Neptune's arcs have optical depths around 0.1 (Smith *et al.*, 1989; Porco *et al.*, 1995), and so collisions among the ring particles cannot be ignored. The primary issue here is that the co-rotation sites correspond to dynamically stable potential maxima, so energy dissipation by inelastic interparticle collisions will cause particles to move away from these sites. Material therefore cannot be confined unless the dissipated energy can be replenished. A nearby and well-separated Lindblad resonance can supply the orbital energy required to maintain ring particle libration around the co-rotation site by exerting repulsive torques on the ring material. The change rate of energy (per unit mass) $\dot{\zeta}$ for particles around co-rotation points, averaged over one libration period T_C, is given by

$$\dot{\zeta} = -\frac{3n_S}{4\pi\sigma a_0^2}\frac{1}{T_C}\int_{T_C} a\frac{d\Gamma}{da}dt, \tag{12.27}$$

where a_0 is the average orbital radius, σ the ring surface density, and $d\Gamma/da$ the torque density, that is, the torque exerted by the satellite per unit radius (Sicardy, 1991). Because of the presence of the term a in front of $d\Gamma/da$, the energy received is proportional to the gradient of the torque density $d^2\Gamma/da^2$. Physically, this means that a given particle must undergo a larger repulsion on the inner side of its libration path than on the outer side, in order to compensate for the spreading effect due to dissipation. Thus, the resulting differential torque across a co-rotation site can serve to stabilize particles and form a stable ring arc.

The exact resonances involved in confining Neptune's arcs have also been debated. The requisite resonances are often attributed to the small nearby satellite Galatea, which has a slightly inclined orbit with $I_G \simeq 0.05$ deg (Owen *et al.*, 1991) and lies only 980 km inside the Adams ring, placing the latter very close to Galatea's 42:43 resonance. After this 150-km wide moon was discovered in Voyager images, Porco (1991) combined the available spacecraft observations with the previously developed theory of Goldreich *et al.* (1986), and suggested that the arcs could be confined by a combination of the 42 : 43 co-rotation *inclination* resonance (CIR) and Lindblad resonance with this moon. Additional detailed simulations (Foryta and Sicardy, 1996; Hanninen and Porco, 1997; Salo and Hänninen, 1998) supported this confinement mechanism. However, subsequent Earth-based and HST observations (Dumas *et al.*, 1999; Sicardy *et al.*, 1999) indicated that the ring arcs are near, but not within, the CIR with Galatea, in agreement with one of the two

possible solutions for the arcs' motion found by Nicholson *et al.* (1995) after a reanalysis of all previous Earth-based occultation data. In 2002 and 2003, adaptive-optics Keck images confirmed the mismatch between the arcs' position and the location of the 42 : 43 CIR (de Pater *et al.*, 2005). The latest Earth-based adaptive optics observations were taken in 2007 at 2.2 μm (K band) with the Very Large Telescope (Renner *et al.*, 2014), re-confirming the mismatch and improving the mean motion values for the arcs and Galatea.

As it became clear that the material could not be trapped in the CIR, Namouni and Porco (2002) suggested that the 42 : 43 co-rotation *eccentricity* resonance (CER) with Galatea could potentially confine material at the arcs' observed semi-major axis, provided those arcs have sufficient mass. This resonance creates 43 potential maxima, each of length 8.37 deg, which does not completely account for the angular lengths of the arcs. The ring mass needed to shift the CER to the arcs' position ($\simeq$ 0.002 Galatea's mass) assumes an eccentricity of 10^{-6} for Galatea and would correspond to a small satellite of 10 km in radius (for a density of $\simeq$ 1 g cm^{-3}). The mass required in this model cannot be contained in a single body since Voyager data excluded undetected satellites of radius larger than 6 km (Smith *et al.*, 1989; Porco *et al.*, 1995). The exact origin of the small residual orbital eccentricity of Galatea, consistent with a forcing by Adams ring's small mass, also still has to be determined.

While models where the arcs are confined by resonances with a single satellite are the most economical, an alternative explanation is that the arcs' confinement involves a small, undetected satellite that can trap dust around its Lagrangian triangular points L_4 or L_5 to form arcs of material (Lissauer, 1985). Since the Lagrangian points are not associated with Lindblad resonances, this model required a second satellite to ensure radial shepherding, and so is more complex than the above models. It turns out that a 6-km-wide icy satellite (near the detection limit of Voyager) would create co-rotation sites with a maximum radial width of about 0.6 km, similar to the CIR sites generated by Galatea, and with a longitudinal extent that encompasses the 40 degrees azimuthal range of the arc system, but without prescribing the observed azimuthal lengths of the four arcs (which are also a challenge for the resonance models).

More recently, Renner *et al.* (2014) have proposed a scenario that generalizes this shepherding theory (Lissauer, 1985; Sicardy and Lissauer, 1992). This model basically assumes that the Adams ring contains a collection of a few moonlets that maintain stable co-orbital relative positions akin to the Lagrangian L_4/L_5 points. Renner and Sicardy (2004) examined the existence of stationary configurations for N co-orbital satellites with small and arbitrary masses. The domains of stable equilibria correspond to configurations where the co-orbitals are either positioned near the L_4 and L_5 points of the most massive satellite, or are grouped near one of these two points. Renner *et al.* (2014) showed how the observed inter-arc regions lead to a limited space of possible masses for the hypothetical satellites that achieve equilibrium. The observed arcs would then be composed of debris trapped between those co-orbital satellites, as shown in the simulation result of Figure 12.20, while Galatea ensures radial shepherding through the 42 : 43 Lindblad resonance. The system of co-orbital satellites is 0.25 km outside the CIR, as given by the observations, and remains stable under the effects of Galatea's perturbations, with a slow libration motion of the moonlets around their equilibrium configuration. Thus, the Adams ring would be in an intermediate situation between a fully collisional ring with only small particles, and a fully accreted system where only one satellite survives after swallowing up all the ring material. Note that the model of Renner *et al.* (2014) naturally explains the observed arc azimuthal lengths as the result of the relative angular positions of the satellites in equilibrium.[4]

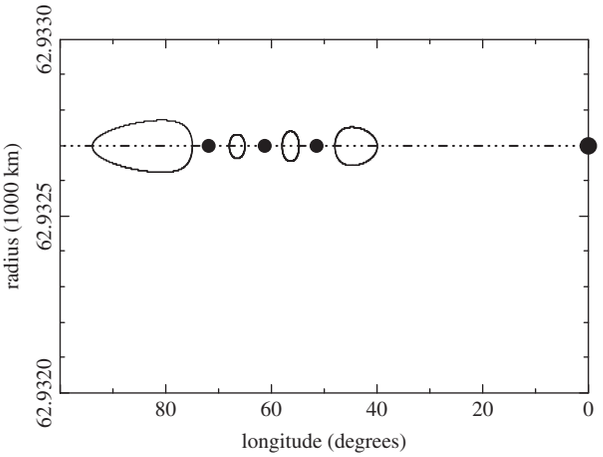

Figure 12.20 Motion of four co-orbital satellites and test particles around Neptune, showing the orbital radius vs longitude in a frame rotating with a satellite S_1 (diameter = 10.5 km, assuming a density of 1 g cm^{-3}). The other satellites S_2, S_3, and S_4 are smaller (diameters around 2.2 km). The co-orbital bodies are in a stable stationary configuration, and the test particles show how arcs of debris can be trapped between these moons (adapted from Renner *et al.* 2014).

Finally, we should note that the observations made since 2002 have revealed that the relative brightness and longitudinal extent of the arcs have changed significantly in recent years (de Pater *et al.*, 2005; Renner *et al.*, 2014). While the three brightest arcs were of comparable brightness during the Voyager encounter, the Liberté arc has largely disappeared in data obtained since 2002, leaving two bright arcs in recent data. Furthermore, more recent observations revealed that the Egalité arc was ∼20% fainter than Fraternité in 2007 suggesting a decrease in intensity that might be as high as ∼44% between 2002 and 2007. Additional data are required to follow the global time evolution of the system, which should provide important clues about the confinement and dynamical evolution of these arcs.

[4] At the 2017 meeting of the Division for Planetary Sciences, Showalter *et al.* presented evidence that these arcs also fall very close to a three-body resonance with the moons Galatea and Larrisa, which would open new dynamical possibilities to explore.

12.3.4 The Dynamics of Denser Dusty Rings

Dusty rings are often assumed to be so tenuous that interactions or collisions among the ring particles can be ignored. While this assumption is likely reasonable for many dusty rings with optical depths below 10^{-5}, like Saturn's E ring, Jupiter's Gossamer rings, and Uranus' μ ring, there are several dusty rings with substantially higher optical depths (see Figure 12.4). As with the arcs in Neptune's Adams ring, interparticle interactions can be important in these denser dusty systems, giving rise to novel structures and unexpected dynamical phenomena. Probably the most extreme example of this is Saturn's F ring, which contains an exceptionally rich diversity of time-variable structures that are discussed in detail in Chapter 13. However, two of the most striking features of the F ring are its surprisingly coherent orbital properties and its many localized brightness enhancements known as clumps. Similar phenomena are observed in other narrow dusty rings, and so comparisons among these systems can help clarify the processes involved in producing these features.

12.3.4.1 The Coherent Shapes of Narrow and Dense Dusty Ringlets

Many narrow dusty rings are non-circular, with the ringlet's distance from the planet's spin axis varying with both longitude and time. For some ringlets, such as Saturn's Charming and D68 ringlets, these variations in the ringlet's radial position match those of a single particle's eccentric orbit (Hedman *et al.*, 2010b, 2014). For other ringlets, like Uranus' λ ring and Saturn's Encke Gap ringlets, the shape is more complex. For the Encke Gap ringlets, each part of the ringlet seems to follow the track of an eccentric orbit, but the parameters of that orbit (its semi-major axis, eccentricity and pericenter position) vary with co-rotating longitude (Hedman *et al.*, 2013). For Uranus' λ ring, the shape of the ringlet appears to include a six-lobed structure similar to the trajectories particles would follow in the vicinity of a Lindblad resonance, although the source of that resonant perturbation has not yet been identified (Showalter, 1995).

In principle, these non-trivial shapes could simply indicate that all the particles in these rings are following similar trajectories because they are being perturbed by the same external forces. For example, there is a component of the Charming ringlet's eccentric shape that can be attributed to solar radiation pressure acting on each of the particles. However, detailed studies of several of Saturn's narrow dusty ringlets reveals some difficulties with this basic picture. For one, these ringlets consist of particles with a range of sizes and, according to Equation (12.13), particles with different sizes should acquire different orbital eccentricities. This would tend to disperse the ring over a range of radii when it is near its orbital pericenter or apocenter, but in reality the observed variations in the Charming ringlet's positions are noticeably larger than its apparent radial width. Furthermore, the shape and alignment of the Charming ringlet relative to the Sun is not constant, but instead varies over time (Hedman *et al.*, 2010b). These changes in the ringlet's shape match the expected changes of a single particle's orbit that would occur if its initial eccentricity and pericenter location did not correspond to the fixed solution described in Section 12.3.1.3 above. In this case the orbital eccentricity can be decomposed into a forced component that maintains a fixed orientation and a "free" component that drifts around the planet at a steady rate determined by the planet's gravitational field (see Chapter 2). Similar "free" eccentricities have been observed in the Encke Gap ringlets (Hedman *et al.*, 2013), and D68's shape seems to match that of a freely precessing orbit with no forced component (Hedman *et al.*, 2014). These coherent motions are somewhat surprising, since any ringlet will consist of particles with a range of semi-major axes, whose orbits should have different precession rates that will become gradually misaligned over time.

The fact that these ringlets do maintain coherent eccentric shapes strongly suggests that some process is forcing the particles within a given part of the ring to have nearly the same orbital elements. In principle, collisions among the ring particles can help align their orbital pericenters, but usually collisions are assumed to cause material to spread in the semi-major axis. Thus it remains unclear exactly how these ringlets preserve their coherent shapes. However, since the most opaque of the dusty rings exhibit this behavior, it is reasonable to expect that interactions among the ring particles, or their collective effects on their environment play an important role.

12.3.4.2 Clumpy Rings

Another interesting aspect of the denser dusty rings is that they can exhibit dramatic longitudinal brightness variations. Besides the arcs in Neptune's Adams ring, significant brightness variations have been reported in Uranus's λ ring, Jupiter's Main ring, and several of Saturn's dusty ringlets, including the F ring. Some of the brightness variations in Saturn's D68 ringlet and Uranus' λ ring are broad-scale and may have some connection with these ringlets' non-trivial shapes (Showalter, 1995; Hedman *et al.*, 2014). However, Jupiter's Main ring, Uranus' λ ring, and the dusty ringlets in Saturn's Encke Gap also contain small-scale brightness enhancements that are often referred to as "clumps" (see Figure 12.21). Some of these clumps could represent debris released by impacts into or among the larger objects in these ringlets, while others may consist of material that is confined by outside forces similar to those that have been invoked to explain the arcs in Neptune's Adams ring. Certainly the proximity of the clumps in Jupiter's ring to the moon Adrastea, and of the Encke Gap ringlets to Saturn's moon Pan, strongly suggest that those moons play some role in sculpting those ringlets. Indeed, the central ringlet in the Encke Gap appears to consist of material that straddles Pan's orbit.

The available data on the clumps in Jupiter's and Uranus' dusty ringlets are unfortunately quite limited. However, Cassini has provided abundant information about the clumps in the Encke Gap ringlets. These observations allow us to observe how the distribution of these clumps changes over time as they slowly drift relative to each other, as well as grow, merge, and dissipate (see Figure 12.22). These data reveal that while the

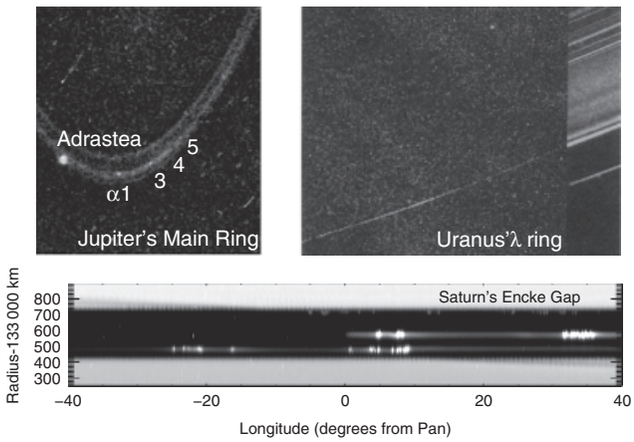

Figure 12.21 Clumps in dusty rings. The image of Jupiter's Main ring from New Horizons (Showalter *et al.*, 2007) shows a series of bright patches near the small moon Amalthea. The Voyager data on Uranus' λ ring (Showalter, 1995) reveals a localized brightness enhancement less than half a degree long. The bottom image is a mosaic of Cassini images showing a complex array of clumps on the ringlets in the Encke Gap (Hedman *et al.*, 2013).

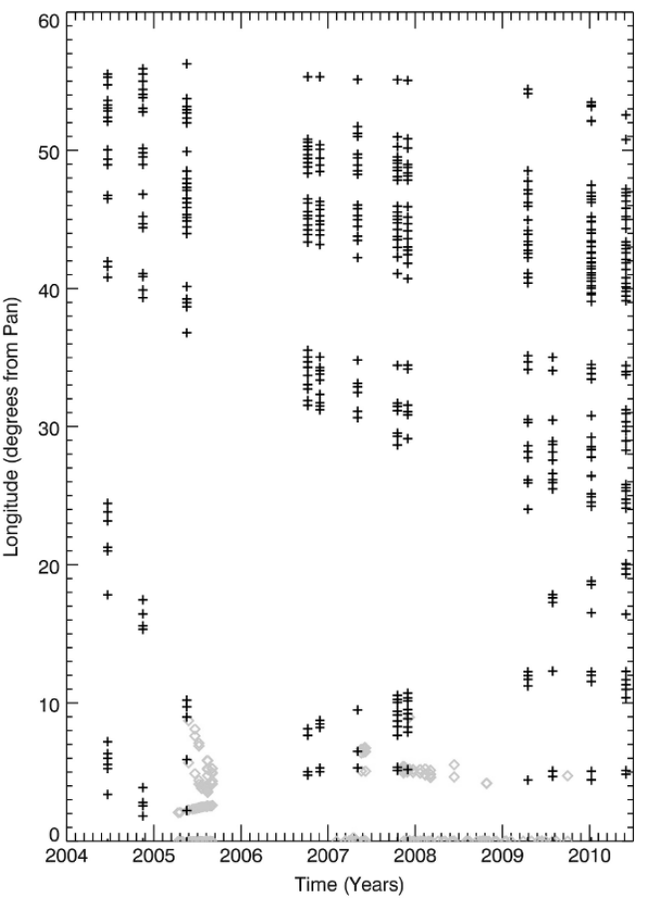

Figure 12.22 Plot showing the positions of the clumps in the Central Encke Gap Ringlet (relative to Pan) over the course of the first six years of the Cassini Mission (black plusses and gray diamonds correspond to different data sets). Note how the clumps are confined to a region just in front of Pan and that within this region the clumps slowly drift relative to each other (adapted from Hedman *et al.*, 2013).

locations of individual clumps can change over time, the overall distribution of clumps is remarkably constant. For example, clumps in the Central Encke Gap ringlet, which consists of material that closely follows the orbit of Saturn's small moon Pan, are only found within 60 degrees of longitude directly in front of that moon (Hedman *et al.*, 2013). This was also the case in the Voyager era (Ferrari and Brahic, 1997), and so this asymmetric clump distribution appears to be a persistent feature of this ringlet. It probably arises from interactions between gravitational perturbations from Pan, non-gravitational forces arising from the planet's magnetosphere, and interactions among the ring particles themselves.

Detailed examinations of the ringlet's orbital properties reveal that, outside the clump-rich region, the mean radius of the Central Encke Gap Ringlet is between 0 and 10 km exterior to Pan's semi-major axis. This implies that the ring particles orbit the planet more slowly than Pan, and so drift backwards relative to the moon. In fact, the mean radius of the particles appears to grow as the particles move further and further downstream of Pan. This trend could be explained if the ringlet particles are experiencing a drag force from their collisions with the planet's magnetospheric plasma. However, as the particles approach the clump-rich region in front of Pan, the average radius of the ringlet falls back to that of Pan's semi-major axis. What may be happening here is that as the particles begin to approach Pan, the moon's gravitational pull will act in the opposite direction to their orbital motion, extracting energy from their orbits and causing them to fall closer to the planet. Normally, this would cause the particles to start to drift forwards relative to Pan so that their trajectories librate around the moon's Lagrange points (following so-called horseshoe orbits). However, in this case the material that tries to move forwards relative to Pan will still feel a drag force and so drift outwards until their semi-major axes are greater than Pan's, causing it to move back towards the moon. The combination of such a drag force with Pan's gravitational perturbations can therefore cause material to become trapped in the region just in front of Pan. Furthermore, material in this region could become concentrated because collisions among particles drifting in opposite directions could slow their relative motions, increasing the local particle density and the probability that further collisions will occur. This could even lead to the creation of clumps, but numerical simulations are needed to properly evaluate these ideas.

12.4 OPEN QUESTIONS AND FUTURE DIRECTIONS

Dusty rings are a rich collection of dynamical systems exhibiting a diverse array of structures and compositions. The currently available data from Earth-based telescopes and spacecraft instruments have provided many important insights into how these rings operate, but there is still much left to learn and understand. Some of the open questions regarding these dusty systems that still need to be answered include the following.

- Why do so many different dusty rings appear to have a feature in their size distribution around a few tens of microns?

- What is the ultimate origin of the multiple compositional classes of particles observed in Saturn's E ring?
- How exactly are the asymmetries in the E ring generated and maintained?
- How are the spokes above Saturn's main ring formed and what phenomena govern how they evolve?
- How are the periodicities observed in Saturn's Roche Division, spokes, and D ring related to each other and to asymmetries in the planet's magnetosphere?
- Precisely how are Neptune's ring arcs confined?
- How do some dusty rings maintain their coherent shapes and structures and what prompts some of these rings to develop long-lived clumps?
- What dynamical phenomena are responsible for the complex array of structures seen in Saturn's D ring, Jupiter's Main ring, and the dusty material surrounding Uranus' main ring system?
- What processes could have caused the changes in the structures of multiple dusty systems (e.g. Neptune's ring arcs, Uranus' ζ ring, Saturn's D ring) over the past few decades?

For the near future, the vast amount of data returned by the Cassini spacecraft will certainly help many of the efforts to answer these and other questions about the dusty rings. The Cassini data are not only important resources for exploring the properties of Saturn's dusty rings, they can also help clarify phenomena observed by other spacecraft in the dusty rings around Jupiter, Uranus and Neptune. At the same time, advances in technology are enabling telescopes on and around Earth to find previously unseen dusty rings and document the long-term evolution of dust-rich structures, while increasingly powerful numerical methods are allowing the dynamics of these systems to be explored in greater and greater detail. Thus there are good reasons to think that our understanding of dusty rings will continue to advance as we await the next mission to the outer solar system that can provide us with a new set of up-close observations and a fresh set of puzzles to ponder.

ACKNOWLEDGEMENTS

M.M.H. and P.D.N. acknowledge support from the Cassini Data Analysis Program Grant NNX15AQ67G, while F.P. acknowledges funding from the German Research Foundation (DFG) projects PO 1015/2-1, 1015/3-1 and 1015/4-1. We thank H. Throop and S. Brooks for providing their published data on Jupiter's rings. M.M.H. and P.D.N. would also like to thank J. A. Burns for training them in the ways of dusty rings.

REFERENCES

Altobelli, N., Postberg, F., Fiege, K., *et al.* 2016. Flux and composition of interstellar dust at Saturn from Cassini's Cosmic Dust Analyser. *Science*, **352**, 312–318.

Andriopoulou, M., Roussos, E., Krupp, N., *et al.* 2012. A noon-to-midnight electric field and nightside dynamics in Saturn's inner magnetosphere, using microsignature observations. *Icarus*, **220**, 503–513.

Andriopoulou, M., Roussos, E., Krupp, N., *et al.* 2014. Spatial and temporal dependence of the convective electric field in Saturn's inner magnetosphere. *Icarus*, **229**, 57–70.

Arridge, C. S., André, N., Khurana, K. K., *et al.* 2011. Periodic motion of Saturn's nightside plasma sheet. *Journal of Geophysical Research (Space Physics)*, **116**, A11205.

Brooks, S. M., Esposito, L. W., Showalter, M. R., and Throop, H. B. 2004. The size distribution of Jupiter's main ring from Galileo imaging and spectroscopy. *Icarus*, **170**, 35–57.

Burns, J. A., Lamy, P. L., and Soter, S. 1979. Radiation forces on small particles in the solar system. *Icarus*, **40**, 1–48.

Burns, J. A., Showalter, M. R., and Morfill, G. E. 1984. The ethereal rings of Jupiter and Saturn. Pages 200–274 of: Greenberg, R. and Brahic, A. (eds.) *Planetary Rings*, University of Arizona Press.

Burns, J. A., Schaffer, L. E., Greenberg, R. J., and Showalter, M. R. 1985. Lorentz resonances and the structure of the Jovian ring. *Nature*, **316**, 115–119.

Burns, J. A., Showalter, M. R., Hamilton, D. P., *et al.* 1999. The formation of Jupiter's faint rings. *Science*, **284**, 1146.

Callegari, N., and Yokohama, T. 2010. Long-term dynamics of Methone, Anthe and Pallene. *Astronomical Union, IAU Symposium*, **263**, 161–166.

Collette, A., Sternovsky, Z., and Horanyi, M. 2014. Production of neutral gas by micrometeoroid impacts. *Icarus*, **227**, 89–93.

Collette, A., Meyer, G., Malaspina, D., and Sternovsky, Z. 2015. Laboratory investigation of antenna signals from dust impacts on spacecraft. *Journal of Geophysical Research (Space Physics)*, **120**, 5298–5305.

Colwell, J. E. 1996. Size distributions of circumplanetary dust. *Advances in Space Research*, **17**, 161–170.

Cooper, N. J., Murray, C. D., Evans, M. W., *et al.* 2008. Astrometry and dynamics of Anthe (S/2007 S 4), a new satellite of Saturn. *Icarus*, **195**, 765–777.

D'Aversa, E., Bellucci, G., Nicholson, P. D., *et al.* 2010. The spectrum of a Saturn ring spoke from Cassini/VIMS. *GRL*, **37**, L01203.

de Pater, I., Martin, S. C., and Showalter, M. R. 2004. Keck near-infrared observations of Saturn's E and G rings during Earth's ring plane crossing in August 1995. *Icarus*, **172**, 446–454.

de Pater, I., Gibbard, S. G., Chiang, E., *et al.* 2005. The dynamic neptunian ring arcs: evidence for a gradual disappearance of Liberté and resonant jump of Courage. *Icarus*, **174**, 263–272.

de Pater, I., Gibbard, S. G., and Hammel, H. B. 2006a. Evolution of the dusty rings of Uranus. *Icarus*, **180**, 186–200.

de Pater, I., Hammel, H. B., Gibbard, S. G., and Showalter, M. R. 2006b. New dust belts of Uranus: One ring, two ring, red ring, blue ring. *Science*, **312**, 92–94.

Dikarev, V. V. 1999. Dynamics of particles in Saturn's E ring: effects of charge variations and the plasma drag force. *A&A*, **346**, 1011–1019.

Dohnanyi, J. S. 1969. Collisional model of asteroids and their debris. *JGR*, **74**, 2531–2554.

Dougherty, M. K., Khurana, K. K., Neubauer, F. M., *et al.* 2006. Identification of a dynamic atmosphere at Enceladus with the Cassini magnetometer. *Science*, **311**, 1406–1409.

Doyle, L. R., and Grun, E. 1990. Radiative transfer modeling constraints on the size of the spoke particles in Saturn's rings. *Icarus*, **85**, 168–190.

Dumas, C., Terrile, R. J., Smith, B. A., Schneider, G., and Becklin, E. E. 1999. Stability of Neptune's ring arcs in question. *Nature*, **400**, 733–735.

Eichhorn, G. 1976. Analysis of the hypervelocity impact process from impact flash measurements. *PSS*, **24**, 771–781.

Eichhorn, G. 1978. Primary velocity dependence of impact ejecta parameters. *PSS*, **26**, 469–471.

El Moutamid, M., Sicardy, B., and Renner, S. 2014. Coupling between corotation and Lindblad resonances in the presence of secular precession rates. *Celestial Dynamics and Dynamical Astronomy*, **118**, 235–252.

Elrod, M. K., Tseng, W.-L., Wilson, R. J., and Johnson, R. E. 2012. Seasonal variations in Saturn's plasma between the main rings and Enceladus. *Journal of Geophysical Research (Space Physics)*, **117**, 3207.

Ferrari, C., and Brahic, A. 1997. Arcs and clumps in the Encke division of Saturn's rings. *PSS*, **45**, 1051–1067.

Fillius, R. W., McIlwain, C. E., and Mogro-Campero, A. 1975. Radiation belts of Jupiter – A second look. *Science*, **188**(May), 465–467.

Foryta, D. W., and Sicardy, B. 1996. The dynamics of the Neptunian Adams ring's arcs. *Icarus*, **123**, 129–167.

French, R. S., Showalter, M. R., Sfair, R., *et al.* 2012. The brightening of Saturn's F ring. *Icarus*, **219**, 181–193.

Fymat, A. L., and Mease, K. D. 1981. Mie forward scattering – Improved semiempirical approximation with application to particle size distribution inversion. *Applied Optics*, **20**, 194–198.

Goertz, C. K., and Morfill, G. 1983. A model for the formation of spokes in Saturn's rings. *Icarus*, **53**, 219–229.

Goldreich, P., Tremaine, S., and Borderies, N. 1986. Towards a theory for Neptune's arc rings. *Astronomical Journal*, **92**, 490–494.

Grün, E., Morfill, G. E., and Mendis, D. A. 1984. Dust-magnetosphere interactions. Pages 275–332 of: *Planetary Rings*. University of Arizona Press.

Grün, E., Fechtig, H., Hanner, M. S., *et al.* 1992. The Galileo dust detector. *Spa. Sci. Rev.*, **60**, 317–340.

Grün, E., Baguhl, M., Hamilton, D. P., *et al.* 1995. Reduction of Galileo and Ulysses dust data. *PSS*, **43**, 941–951.

Grün, E., Baguhl, M., Hamilton, D. P., *et al.* 1996. Constraints from Galileo observations on the origin of jovian dust streams. *Nature*, **381**, 395–398.

Gurnett, D. A., and Kurth, W. S. 1995. Plasma waves and related phenomena in the magnetosphere of Neptune. Pages 389–423 of: Cruikshank, D. P., Matthews, M. S., and Schumann, A. M. (eds.), *Neptune and Triton*. University of Arizona Press.

Gurnett, D. A., Kurth, W. S., Scarf, K. L., Burns, J. A., and Cuzzi, J. N. 1987. Micron-sized particle impacts detected near Uranus by the Voyager 2 plasma wave instrument. *JGR*, **92**, 14 959–14 968.

Gurnett, D. A., Kurth, W. S., Granroth, L. J., Allendorf, S. C., and Poynter, R. L. 1991. Micron-sized particles detected near Neptune by the Voyager 2 plasma wave instrument. *JGR*, **96**, 19.

Hamilton, D. P. 1993. Motion of dust in a planetary magnetosphere – Orbit-averaged equations for oblateness, electromagnetic, and radiation forces with application to Saturn's E ring. *Icarus*, **101**, 244–264.

Hamilton, D. P. 1994. A comparison of Lorentz, planetary gravitational, and satellite gravitational resonances. *Icarus*, **109**(June), 221–240.

Hamilton, D. P. 1996. The asymmetric time-variable rings of Mars. *Icarus*, **119**, 153–172.

Hamilton, D. P., and Burns, J. A. 1993. Ejection of dust from Jupiter's gossamer ring. *Nature*, **364**, 695–699.

Hamilton, D. P., and Burns, J. A. 1994. Origin of Saturn's E ring: Self-sustained, naturally. *Science*, **264**, 550–553.

Hamilton, D. P., and Krüger, H. 2008. The sculpting of Jupiter's gossamer rings by its shadow. *Nature*, **453**, 72–75.

Hamilton, D. P., Skrutskie, M. F., Verbiscer, A. J., and Masci, F. J. 2015. Small particles dominate Saturn's Phoebe ring to surprisingly large distances. *Nature*, **522**, 185–187.

Hanninen, J., and Porco, C. 1997. Collisional simulations of Neptune's ring arcs. *Icarus*, **126**, 1–27.

Hansen, C. J., Esposito, L., Stewart, A. I. F., *et al.* 2006. Enceladus' water vapor plume. *Science*, **311**, 1422–1425.

Hedman, M. M., and Showalter, M. R. 2016. A new pattern in Saturn's D ring created in late 2011. *Icarus*, **279**, 155–165.

Hedman, M. M., and Stark, C. C. 2015. Saturn's G and D rings provide nearly complete measured scattering phase functions of nearby debris disks. *ApJ*, **811**, 67.

Hedmann, M. M., Burns, J. A., Showalter, M. R., *et al*. 2007a. Saturn's dynamic D ring. *Icarus*, **188**, 89–107.

Hedman, M. M., Burns, J. A., Tiscareno, M. S., *et al.* 2007b. The source of Saturn's G ring. *Science*, **317**, 653–656.

Hedman, M. M., Murray, C. D., Cooper, N. J., *et al.* 2009a. Three tenuous rings/arcs for three tiny moons. *Icarus*, **199**, 378–386.

Hedman, M. M., Burns, J. A., Tiscareno, M. R. and Porco, C. C. 2009b. Organizing some very tenuous things: Resonant structures in Saturn's faint rings. *Icarus*, **202**, 260–279.

Hedman, M. M., Nicholson, P. D., Showalter, M. R., *et al*. 2009c. Spectral observations of the Enceladus Plume with Cassini-VIMS. *The Astrophysical Journal*, **693**, 1749–1762.

Hedman, M. M., Cooper, N. J., Murray, C. D., 2010a. Aegaeon (Saturn LIII), a G-ring object. *Icarus*, **207**, 433–447.

Hedman, M. M., Burt, J. A., Burns, J. A., and Tiscareno, M. S. 2010b. The shape and dynamics of a heliotropic dusty ringlet in the Cassini Division. *Icarus*, **210**, 284–297.

Hedman, M. M., Burns, J. A., Evans, M. W., Tiscareno, M. S., and Porco, C. C. 2011a. Saturn's curiously corrugated C ring. *Science*, **332**, 708–711.

Hedman, M. M., Nicholson, P. D., Showalter, M. R., *et al.* 2011b. The Christiansen Effect in Saturn's narrow dusty rings and the spectral identification of clumps in the F ring. *Icarus*, **215**, 695–711.

Hedman, M. M., Burns, J. A., Hamilton, D. P., and Showalter, M. R. 2012. The three-dimensional structure of Saturn's E ring. *Icarus*, **217**, 322–338.

Hedman, M. M., Burns, J. A., Hamilton, D. P., and Showalter, M. R. 2013. Of horseshoes and heliotropes: Dynamics of dust in the Encke Gap. *Icarus*, **223**, 252–276.

Hedman, M. M., Burt, J. A., Burns, J. A., and Showalter, M. R. 2014. Non-circular features in Saturn's D ring: D68. *Icarus*, **233**, 147–162.

Hedman, M. M., Burns, J. A., and Showalter, M. R. 2015. Corrugations and eccentric spirals in Saturn's D ring: New insights into what happened at Saturn in 1983. *Icarus*, **248**, 137–161.

Hill, T. W., Thomsen, M. F., Tokar, R. L., *et al.* 2012. Charged nanograins in the Enceladus plume. *Journal of Geophysical Research (Space Physics)*, **117**, A05209.

Hillier, J. K., Green, S. F., McBride, N., *et al.* 2007a. Interplanetary dust detected by the Cassini CDA Chemical Analyser. *Icarus*, **190**, 643–654.

Hillier, J. K., Green, S. F., McBride, N., *et al.* 2007b. The composition of Saturn's E ring. *Mon. Not. Roy. Ast. Soc.*, **377**, 1588–1596.

Horányi, M., and Burns, J. A. 1991. Charged dust dynamics – Orbital resonance due to planetary shadows. *Journal of Geophysical Research*, **96**, 19.

Horányi, M., and Juhász, A. 2000. Dynamics and distribution of Saturn's E ring particles. *AAS/Division for Planetary Sciences Meeting*, **32**.

Horányi, M., Burns, J. A., and Hamilton, D. P. 1992. The dynamics of Saturn's E ring particles. *Icarus*, **97**, 248–259.

Horányi, M., Morfill, G., and Grün, E. 1993. Mechanism for the acceleration and ejection of dust grains from Jupiter's magnetosphere. *Nature*, **363**, 144–146.

Horányi, M., Juhász, A., and Morfill, G. E. 2008. Large-scale structure of Saturn's E-ring. *GRL*, **35**, L04203.

Hsu, H.-W., Kempf, S., Postberg, F., *et al.* 2011. Cassini dust stream particle measurements during the first three orbits at Saturn. *Journal of Geophysical Research (Space Physics)*, **116**, A08213.

Hsu, H.-W., Krüger, H., and Postberg, F. 2012. Dynamics, composition, and origin of jovian and saturnian dust-stream particles. Page 77 of: Mann, I., Meyer-Vernet, N., and Czechowski, A. (eds.), *Nanodust in the Solar System: Discoveries and Interpretations*. Astrophysics and Space Science Library, vol. 385.

Hsu, H.-W., Postberg, F., Sekine, Y., *et al.* 2015. Ongoing hydrothermal activities within Enceladus. *Nature*, **519**, 207–210.

Hubbard, W. B., Brahic, A., Sicardy, B., *et al.* 1986. Occultation detection of a Neptunian ring-like arc. *Nature*, **319**, 636–640.

Humes, D. H., Alvarez, J. M., O'Neal, R. L., and Kinard, W. H. 1974. The interplanetary and near-Jupiter meteoroid environments. *JGR*, **79**, 3677.

Ingersoll, A. P., and Ewald, S. P. 2011. Total particulate mass in Enceladus plumes and mass of Saturn's E ring inferred from Cassini ISS images. *Icarus*, **216**, 492–506.

Jackson, J. D. 1998. *Classical Electrodynamics*, 3rd edition. New York, John Wiley & Sons.

Jones, G. H., Krupp, N., Krüger, H., *et al.* 2006. Formation of Saturn's ring spokes by lightning-induced electron beams. *GRL*, **33**, L21202.

Jones, G. H., Roussos, E., Krupp, N., *et al.* 2008. The dust halo of Saturn's largest icy moon: Evidence of rings at Rhea? *Science*, **319**, 1380–1384.

Juhász, A., and Horányi, M. 2004. Seasonal variations in Saturn's E-ring. *GRL*, **31**, 19703.

Juhász, A., Horányi, M., and Morfill, G. E. 2007. Signatures of Enceladus in Saturn's E ring. *GRL*, **34**, 9104.

Jurac, S., Johnson, R. E., and Richardson, J. D. 2001. Saturn's E ring and production of the neutral torus. *Icarus*, **149**, 384–396.

Kempf, S., Srama, R., Postberg, F., *et al.* 2005a. Composition of saturnian stream particles. *Science*, **307**, 1274–1276.

Kempf, S., Srama, R., Horányi, M., *et al.* 2005b. High-velocity streams of dust originating from Saturn. *Nature*, **433**, 289–291.

Kempf, S., Beckmann, U., Srama, R., *et al.* 2006. The electrostatic potential of E ring particles. *PSS*, **54**, 999–1006.

Kempf, S., Beckmann, U., Moragas-Klostermeyer, G., *et al.* 2008. The E ring in the vicinity of Enceladus I: Spatial distribution and properties of the ring particles. *Icarus*, **193**, 420–437.

Kempf, S., Beckmann, U., and Schmidt, J. 2010. How the Enceladus dust plume feeds Saturn's E ring. *Icarus*, **206**, 446–457.

Khawaja, N., Postberg, F., Reviol, R., and Srama, R. 2015. Characterization of signatures from organic compounds in CDA mass spectra of ice particles in Saturn's E-ring. Page 12799 of: *EGU General Assembly Conference Abstracts*. EGU General Assembly Conference Abstracts, vol. 17.

Kinard, W. H., O'Neal, R. L., Alvarez, J. M., and Humes, D. H. 1974. Interplanetary and near-Jupiter meteoroid environments: Preliminary results from the meteoroid detection experiment. *Science*, **183**, 321–322.

Krüger, H., Grün, E., Graps, A., *et al.* 2001. One year of Galileo dust data from the Jovian system: 1996. *PSS*, **49**, 1285–1301.

Krüger, H., Bindschadler, D., Dermott, S. F., *et al.* 2006. Galileo dust data from the jovian system: 1997 1999. *PSS*, **54**, 879–910.

Krüger, H., Hamilton, D. P., Moissl, R., and Grün, E. 2009. Galileo in-situ dust measurements in Jupiter's gossamer rings. *Icarus*, **203**, 198–213.

Kurth, W. S., Averkamp, T. F., Gurnett, D. A., and Wang, Z. 2006. Cassini RPWS observations of dust in Saturn's E Ring. *PSS*, **54**, 988–998.

Lissauer, J. J. 1985. Shepherding model for Neptune's arc ring. *Nature*, **318**, 544.

McGhee, C. A., French, R. G., Dones, L., *et al.* 2005. HST observations of spokes in Saturn's B ring. *Icarus*, **173**, 508–521.

McNutt, R. L., Selesnick, R. S., and Richardson, J. D. 1987. Low-energy plasma observations in the magnetosphere of Uranus. *JGR*, **92**, 4399–4410.

Menietti, J. D., Gurnett, D. A., and Groene, J. B. 2005. Radio emission observed by Galileo in the inner Jovian magnetosphere during orbit A-34. *Planetary and Space Science*, **53**, 1234–1242.

Meyer-Vernet, N., Aubier, M. G., and Pedersen, B. M. 1986. Voyager 2 at Uranus – Grain impacts in the ring plane. *GRL*, **13**, 617–620.

Mitchell, C. J., Porco, C. C., Dones, H. L., and Spitale, J. N. 2013. The behavior of spokes in Saturn's B ring. *Icarus*, **225**, 446–474.

Morfill, G. E., and Gruen, E. 1979. The motion of charged dust particles in interplanetary space. I – The zodiacal dust cloud. II – Interstellar grains. *Planetary and Space Sciences*, **27**, 1269–1292.

Morfill, G. E., Havnes, O., and Goertz, C. K. 1993. Origin and maintenance of the oxygen torus in Saturn's magnetosphere. *JGR*, **98**, 11 285.

Namouni, F., and Porco, C. 2002. The confinement of Neptune's ring arcs by the moon Galatea. *Nature*, **417**, 45–47.

Nicholson, P. D., Mosqueira, I., and Matthews, K. 1995. Stellar occultation observations of Neptune's rings: 1984-1988. *Icarus*, **113**, 295–330.

Nicholson, P. D., Showalter, M. R., and Dones, L. 1996. Observations of Saturn's ring-plane crossing in August and November. *Science*, **272**, 509–516.

Owen, W. M., Vaughan, R. M., and Synnott, S. P. 1991. Orbits of the six new satellites of Neptune. *Astronomical Journal*, **101**, 1511–1515.

Persoon, A. M., Gurnett, D. A., Leisner, J. S., *et al.* 2013. The plasma density distribution in the inner region of Saturn's magnetosphere. *Journal of Geophysical Research (Space Physics)*, **118**, 2970–2974.

Porco, C. A., and Danielson, G. E. 1982. The periodic variation of spokes in Saturn's rings. *AJ*, **87**, 826–833.

Porco, C. C. 1991. An explanation for Neptune's ring arcs. *Science*, **253**, 995–1001.

Porco, C. C., Nicholson, P. D., Cuzzi, J. N., Lissauer, J. J., and Esposito, L. W. 1995. Neptune's ring system. In Cruikshank, D. P., Matthews, M. S., and Schumann, A. M. (eds.), *Neptune and Triton*. University of Arizona Press.

Porco, C. C., Baker, E., Barbara, J., *et al.* 2005. Cassini imaging science: Initial results on Saturn's rings and small satellites. *Science*, **307**, 1226–1236.

Porco, C. C., Helfenstein, P., Thomas, P. C., *et al.* 2006. Cassini observes the active south pole of Enceladus. *Science*, **311**, 1393–1401.

Postberg, F., Kempf, S., Srama, R., *et al.* 2006. Composition of jovian dust stream particles. *Icarus*, **183**, 122–134.

Postberg, F., Kempf, S., Hillier, J. K., *et al.* 2008. The E-ring in the vicinity of Enceladus II: Signatures of Enceladus in the elemental composition of E-ring particles. *Icarus*, **193**, 438–454.

Postberg, F., Kempf, S., Schmidt, J., *et al.* 2009. Sodium salts in E-ring ice grains from an ocean below the surface of Enceladus. *Nature*, **459**, 1098–1101.

Postberg, F., Schmidt, J., Hillier, J., Kempf, S., and Srama, R. 2011. A salt-water reservoir as the source of a compositionally stratified plume on Enceladus. *Nature*, **474**, 620–622.

Postberg, F., Khwaja, N., Kempf, S., *et al.* 2017. Complex organic macromolecular compounds in ice grains from Enceladus. *LPSC abstracts*. **48**, 1401.

Renner, S., and Sicardy, B. 2004. Stationary configurations for co-orbital satellites with small arbitrary masses. *Celestial Mechanics and Dynamical Astronomy*, **88**, 397–414.

Renner, S., Sicardy, B., Souami, D., Carry, B., and Dumas, C. 2014. Neptune's ring arcs: VLT/NACO near-infrared observations and a model to explain their stability. *Astronomy and Astrophysics*, **563**, A133.

Roussos, E., Jones, G. H., Krupp, N., *et al.* 2008. Energetic electron signatures of Saturn's smaller moons: Evidence of an arc of material at Methone. *Icarus*, **193**, 455–464.

Salo, H., and Hänninen, J. 1998. Neptune's partial rings: Action of Galatea on self-gravitating arc particles. *Science*, **282**, 1102–1104.

Schmidt, J., Brilliantov, N., Spahn, F., and Kempf, S. 2008. Slow dust in Enceladus' plume from condensation and wall collisions in tiger stripe fractures. *Nature*, **451**, 685–688.

Sekine, Y., Shibuya, T., Postberg, F., *et al.* 2015. High-temperature water–rock interactions and hydrothermal environments in the chondrite-like core of Enceladus. *Nature Communications*, **6**, 8604.

Selesnick, R. S., and McNutt, Jr., R. L. 1987. Voyager 2 plasma ion observations in the magnetosphere of Uranus. *JGR*, **92**, 15249–15262.

Showalter, M. R. 1995. Arcs and clumps in the Uranian λ ring. *Science*, **267**, 490–493.

Showalter, M. R. 1996. Saturn's D ring in the Voyager images. *Icarus*, **124**, 677–689.

Showalter, M. R., and Lissauer, J. J. 2006. The second ring-moon system of Uranus: Discovery and dynamics. *Science*, **311**, 973–977.

Showalter, M. R., Cheng, A. F., Weaver, H. R., *et al*. 2007. Clump detection and limits on moons in Jupiter's ring system. *Science*, **318**, 232–234.

Showalter, M. R., de Pater, I., Verbanac, G., Hamilton, D. P., and Burns, J. A. 2008. Properties and dynamics of Jupiter's gossamer rings from Galileo, Voyager, Hubble and Keck images. *Icarus*, **195**, 361–377.

Showalter, M. R., Hedman, M. M., and Burns, J. A. 2011. The impact of comet Shoemaker-Levy 9 sends ripples through the rings of Jupiter. *Science*, **332**, 711.

Shu, F. H. 1984. Waves in planetary rings. Pages 513–561 of: *Planetary Rings*, University of Arizona Press.

Sicardy, B. 1991. Numerical exploration of planetary arc dynamics. *Icarus*, **89**, 197–219.

Sicardy, B., and Lissauer, J. J. 1992. Dynamical models of the arcs in Neptune's 63K ring (1989N1R). *Advances in Space Research*, **12**, 81–95.

Sicardy, B., Roddier, F., Roddier, C., *et al.* 1999. Images of Neptune's ring arcs obtained by a ground-based telescope. *Nature*, **400**, 731–733.

Smith, B. A., Soderblom, L. A., Banfield, D., *et al.* 1989. Voyager 2 at Neptune – Imaging science results. *Science*, **246**, 1422–1449.

Spahn, F., Schmidt, J., Albers, N., *et al.* 2006a. Cassini dust measurements at Enceladus and implications for the origin of the E ring. *Science*, **311**, 1416–1418.

Spahn, F., Schmidt, J., Albers, N., *et al.* 2006b. Cassini dust measurements at Enceladus and implications for the origin of the E ring. *Science*, **311**, 1416–1418.

Spitale, J. N., Jacobson, R. A., Porco, C. C., and Owen, Jr., W. M. 2006. The orbits of Saturn's small satellites derived from combined historic and Cassini imaging observations. *Astronomical Journal*, **132**, 692–710.

Srama, R., Kempf, S., Moragas-Klostermeyer, G., *et al.* 2006. In situ dust measurements in the inner Saturnian system. *PSS*, **54**, 967–987.

Srama, R., Kempf, S., Moragas-Klostermeyer, G., *et al.* 2011. The cosmic dust analyser onboard cassini: ten years of discoveries. *CEAS Space Journal*, **2**, 3–16.

Sun, K. L., Seiss, M., Hedmann, M. M., and Spatin, F. 2017. Dust in the arcs of Methone and Anthe. *Icarus*, **284**, 206–215.

Tamayo, D., Burns, J. A., Hamilton, D. P., and Hedman, M. M. 2011. Finding the trigger to Iapetus' odd global albedo pattern: Dynamics of dust from Saturn's irregular satellites. *Icarus*, **215**, 260–278.

Tamayo, D., Markham, S. R., Hedman, M. M., Burns, J. A., and Hamilton, D. P. 2016. Radial profiles of the Phoebe ring: A vast debris disk around Saturn. *Icarus*, **275**, 117–131.

Throop, H. B., Porco, C. C., West, R. A., *et al.* 2004. The jovian rings: new results derived from Cassini, Galileo, Voyager, and Earth-based observations. *Icarus*, **172**, 59–77.

Tiscareno, M. S., Mitchell, C. J., Murray, C. D., *et al.* 2013. Observations of ejecta clouds produced by impacts onto Saturn's rings. *Science*, **340**, 460–464.

Vahidinia, S., Cuzzi, J. N., Hedman, M., *et al.* 2011. Saturn's F ring grains: Aggregates made of crystalline water ice. *Icarus*, **215**, 682–694.

van Allen, J. A. 1982. Findings on rings and inner satellites of Saturn of Pioneer 11. *Icarus*, **51**, 509–527.

van Allen, J. A. 1983. Absorption of energetic protons by Saturn's Ring G. *JGR*, **88**, 6911–6918.

van Allen, J. A. 1987. An upper limit on the sizes of shepherding satellites at Saturn's ring G. *JGR*, **92**, 1153–1159.

van de Hulst, H. C. 1957. *Light Scattering by Small Particles*. New York, John Wiley & Sons.

Verbiscer, A. J., Skrutskie, M. F., and Hamilton, D. P. 2009. Saturn's largest ring. *Nature*, **461**, 1098–1100.

Waite, J. H., Combi, M. R., Ip, W.-H., *et al.* 2006. Cassini ion and neutral mass spectrometer: Enceladus plume composition and structure. *Science*, **311**, 1419–1422.

Wang, Z., Gurnett, D. A., Averkamp, T. F., Persoon, A. M., and Kurth, W. S. 2006. Characteristics of dust particles detected near Saturn's ring plane with the Cassini Radio and Plasma Wave instrument. *PSS*, **54**, 957–966.

Wilson, R. J., Bagenal, F., Delamere, P. A., *et al.* 2013. Evidence from radial velocity measurements of a global electric field in Saturn's inner magnetosphere. *Journal of Geophysical Research (Space Physics)*, **118**, 2122–2132.

Ye, S.-Y., Gurnett, D. A., Kurth, W. S., *et al.* 2014. Properties of dust particles near Saturn inferred from voltage pulses induced by dust impacts on Cassini spacecraft. *Journal of Geophysical Research (Space Physics)*, **119**, 6294–6312.

Ye, S.-Y., Gurnett, D. A., and Kurth, W. S. 2016. In-situ measurements of Saturn's dusty rings based on dust impact signals detected by Cassini RPWS. *Icarus*, **279**, 51–61.

Yeoh, S. K., Chapman, T. A., Goldstein, D. B., Varghese, P. L., and Trafton, L. M. 2015. On understanding the physics of the

Enceladus south polar plume via numerical simulation. *Icarus*, **253**, 205–222.

Zeehandelaar, D. B., and Hamilton, D. P. 2007. A local source for the Pioneer 10 and 11 circumjovian dust detections. *Dust in Planetary Systems*, **643**, 103–106.

Zolotov, M. Y. 2007. An oceanic composition on early and today's Enceladus. *GRL*, **34**, 23203.

Zook, H. A., and Su, S.-Y. 1982. Dust particles in the Jovian system. Pages 893–894 of: *Lunar and Planetary Science Conference*. Lunar and Planetary Science Conference, vol. 13.

Zook, H.A., Grün, E., Baguhl, M., *et al.* 1996. Solar wind magnetic field bending of Jovian dust trajectories. *Science*, **274**, 1501–1503.